



Very High Spatial Resolution Downscaled SMAP Radiometer Soil Moisture in the CONUS Using VIIRS/MODIS Data

Bin Fang , Venkat Lakshmi , *Senior Member, IEEE*, Michael H. Cosh, *Senior Member, IEEE*, and Christopher Hain, *Senior Member, IEEE*

Abstract—Satellite remote sensing has been providing passive microwave soil moisture (SM) retrievals of a global spatial coverage and a high revisit frequency for research and applications in earth and environmental sciences, specifically after the soil moisture active and passive (SMAP) was launched in 2015. But, the spatial resolution of SM data is restricted to tens of kilometers, which is insufficient for regional or watershed scale studies. In this article, an SM downscaling algorithm was developed based on the vegetation modulated apparent thermal inertia relationship between SM and changes in land surface temperature (LST). The algorithm used data sets from the North America Land Data Assimilation System Noah model outputs and the advanced very high resolution radiometer data of the long term data record from 1981 to 2018. Here, the downscaling model was applied to visible/infrared LST data from the visible infrared imaging radiometer suite at 400-m and the moderate resolution imaging spectroradiometer at 1 km to downscale the L2 radiometer half-orbit 9 km SMAP SM from 2018 to 2019 for the contiguous United States. The 400-m/1-km downscaled SM products were validated using 125 *in situ* SM ground measurements acquired from the International Soil Moisture Network. The validation results summarized by SM network show that the overall unbiased RMSE for 400-m of the improved/original downscaling algorithms and 1-km SM outperform 9-km SM by 0.01, 0.007, and 0.012 m³/m³ volumetric soil moisture, respectively, which indicates a fairly good performance of the downscaling algorithm. It is also found that precipitation has an impact on the 9-km SMAP SM.

Index Terms—Downscaling algorithm, moderate resolution imaging spectroradiometer (MODIS), North America Land Data Assimilation System (NLDAS), soil moisture active and passive (SMAP), visible infrared imaging radiometer suite (VIIRS).

I. INTRODUCTION

SOIL moisture is described as the water content of the soil layer and generally in the case of remote sensing, this is

Manuscript received December 12, 2020; revised February 15, 2021 and April 6, 2021; accepted April 21, 2021. Date of publication April 27, 2021; date of current version May 26, 2021. This work was supported in part by the U.S. Department of Agriculture, Agricultural Research Service. (*Corresponding author: Bin Fang.*)

Bin Fang is with the Engineering Systems and Environment, University of Virginia, Charlottesville, VA 22902 USA (e-mail: bf3fh@virginia.edu).

Venkat Lakshmi is with the Department of Engineering Systems and the Environment, University of Virginia, Charlottesville, VA 22902 USA (e-mail: vlakshmi@virginia.edu).

Michael H. Cosh is with the USDA Agricultural Research Service, Hydrology and Remote Sensing Laboratory, Beltsville, MD 20705 USA (e-mail: michael.cosh@usda.gov).

Christopher Hain is with the NASA, Marshall Space Flight Center, Huntsville, AL 35808 USA (e-mail: christopher.hain@nasa.gov).

Digital Object Identifier 10.1109/JSTARS.2021.3076026

restricted to the top few centimeters of depth. Soil moisture is an important variable for studying land surface processes, water and heat flux exchanges and interactions between land and atmosphere. It is also a key input variable in land surface models (LSMs) for numerous studies in hydrology, agriculture, climatology, weather forecasting, and ecology. Remote sensing techniques have been providing global coverage soil moisture (SM) retrievals from passive microwave satellite sensor observations in recent decades [1]–[3]. Compared with the traditional methods of measuring SM from ground networks or field surveys, remotely sensed SM can provide regularly available (on the order of 1–2 days revisit), higher spatial/temporal resolutions (as ground observations are sparse) with reliable quality [4]–[6]. The satellites which have retrieved SM measurements from passive microwave frequency brightness temperature (T_B) observations include: Advanced Microwave Scanning Radiometer for the Earth Observing System onboard National Aeronautics and Space Administration's (NASA) Aqua satellite [7]–[9], Advanced Microwave Scanning Radiometer 2 (AMSR2) onboard Japan Aerospace Exploration Agency's (JAXA) Global Change Observation Mission - Water (GCOM-W1) satellite [10]–[13], European Space Agency's soil moisture and ocean salinity satellite [14]–[16], NASA's Soil Moisture Active/Passive (SMAP) [17]–[20], and aquarius sensor onboard Argentine Satellite de Aplicaciones Cientificas-D spacecraft [21], [22]. The L-band microwave T_B observations are favored to provide top surface SM retrievals (0–5 cm depth) with reliable accuracy [23]–[26]. Specifically, the radio frequency interference effect on L-band observations can be effectively mitigated through various approaches when the SMAP data are available [27]–[29]. In this article, the SMAP SM were produced by the single channel algorithm (SCA), which used T_B observations at both horizontal and vertical polarizations [1].

Presently, due to the limitation of antenna diameter size, the spatial resolution of all available microwave radiometer SM retrievals is only on the order of tens of kilometers, which cannot satisfy the requirement of hydrological or agricultural studies at finer scales [2], [30]. To solve this problem, many studies focused on developing approaches to improve the spatial resolution of SM products [31], [32]. These downscaling algorithms can be summarized as three main types: Integrate satellite observations from multiple platforms. Some of the studies utilized the high-resolution data from optical/thermal bands

[33]–[38] or radar sensors [39]–[44] to downscale microwave SM retrievals. Use other SM related geophysical variable data of high resolution, such as topography, soil surface properties or vegetation properties [45]–[52]. Use mathematical modeling. There are many studies that developed downscaling algorithms based on statistical approaches or data assimilation technique [53]–[57].

In this article, an ATI principle-based SM downscaling algorithm was built and implemented to downscale the enhanced 9-km SMAP radiometer only SM product from 2018 to 2019 in the CONUS, by using high resolution visible/infrared (VIS/IR) data of visible infrared imaging radiometer suite (VIIRS) (400 m) and moderate resolution imaging spectroradiometer (MODIS) (1 km). The downscaled SMAP SM were validated by *in situ* SM ground measurements from three observational networks. The detailed description of this downscaling algorithm is introduced in the article by [35]. The original algorithm referred to the universal triangle relationship between SM, LST, and vegetation and was developed based on the vegetation modulated relationship between SM and change in LST [58]–[64]. A major improvement of this algorithm was also conducted, which applied downscaling of the SMAP SM on an extended 33-km domain, instead of the original 9-km grid. This algorithm can efficiently produce routinely available, high spatial resolution and wide coverage SMAP SM products by only utilizing the VIS/IR band products from VIIRS/MODIS [65]–[69].

The original contributions of this article include the following.

- 1) The new algorithm improves the downscaling step on the extended grid at 33 km for minimizing the sharp edge effect presented in the downscaled SM products.
- 2) For the first time, the SM downscaling algorithm was applied on the VIIRS LST and leaf area index (LAI) data to produce the downscaled SM data of higher spatial resolution at 400 m than that of the previous downscaled SM products.
- 3) We also compared, analyzed, and discussed the SM data and validation results of different scales at 400 m, 1 km, as well as 9 km in CONUS.

II. METHOD

The 400-m/1-km resolution SM products were derived from the downscaling algorithm [35], which is based on the ATI relationship between SM and LST change. An assumption was made that there is a negative correlation between SM of top-soil surface and LST change rate during a given time period [70]. This correlation is higher in spring/summer months (April–September) in Northern Hemisphere, when the evapotranspiration is high. Hence, the maximal diurnal LST differences can be approximated by the LST differences between two VIIRS or Aqua MODIS overpasses 1:30 P.M. and 1:30 A.M., which correspond to the average times of maximum and minimum temperatures in a day, respectively. The LST differences between 1:30 A.M./P.M. also correspond to SMAP overpasses 6:00 A.M./P.M. To build the downscaling algorithm, the long-term relationship between two NLDAS Noah model output variables: surface skin temperature differences ΔT_s between 1:30 A.M./P.M. and SM θ of 0–10 cm soil layer at 6:00 A.M./P.M. from 1981–2018 was

modeled using linear regression equation, as

$$\theta(i, j) = a_0 + a_1 \Delta T_s(i, j) \quad (1)$$

where, a_0 and a_1 are the linear regression coefficients for the modeled $\theta - \Delta T_s$ relationship of MODIS/VIIRS grid (i, j) , respectively.

Additionally, the VIIRS LAI and long term data record (LTDR) normalized difference vegetation index (NDVI), which normally range between 0 and 1, were indexed to ten classes with an interval of 0.1. The ΔT_s and θ within any NLDAS grid were classified into ten classes, based on their corresponding NDVI indices. Therefore, ten modeled $\theta - \Delta T_s$ relationship equations could be generated corresponding to each NLDAS grid. All the MODIS/VIIRS grids of ΔT_s , which were included by one NLDAS grid would be applied to the proper equations determined by the corresponding LAI/NDVI values to calculate SM at 400 m/1 km. There was an assumption made that the $\theta - \Delta T_s$ equation of any NLDAS grid could summarize and represent the ATI relationship of all VIIRS/MODIS grids within that NLDAS grid. A past study showed the spatially averaged ATI and soil water indicators were highly related at the watershed scale [71]. In addition to this, the following downscaling step will correct the biases of the $\theta - \Delta T_s$ model outputs, which are induced by the assumption.

In order to remove the inconsistency between the SMAP radiometer SM, and VIIRS/MODIS ΔT_s data calculated SM, which were derived from T_B observations of different satellite sensors and spectral bands: microwave L-band radiometer and VIS/IR spectroradiometer, the downscaling equation was applied. The difference between any single 9-km SMAP SM grid and VIIRS/MODIS grids of calculated SM corresponding to that SMAP grid, was calculated to correct the SM calculated from (1), as

$$\theta^c(i, j) = \theta(i, j) + \left[\Theta - \frac{1}{n} \sum \theta_n \right] \quad (2)$$

where θ^c is the adjusted SMAP SM of MODIS/VIIRS grid (i, j) , Θ is the 9-km SMAP SM grid. θ_n are the n of MODIS/VIIRS grids of calculated SM corresponding to Θ at a 33-km domain, which is extended from the original 9-km resolution.

This step can include more MODIS/VIIRS grids within the boundaries of the 33-km grid and it can efficiently smooth the sharp edge issue induced by SMAP or NLDAS grid boundaries. It can be considered as a major improvement of the original algorithm.

III. DATASETS

Details of the datasets used in this study for building, implementing and validating the SM downscaling algorithm are given in Table I.

A. Soil Moisture Active and Passive (SMAP)

The SMAP is a near-polar sun synchronous orbit satellite which has an L-band radiometer (1.41 GHz). It was developed and launched by NASA in January 2015. The SMAP has a 2-3 day revisit frequency and two overpasses at local time 6 A.M./6 P.M. The SMAP SM are retrieved from the radiometer

TABLE I
DESCRIPTIONS OF THE DATASETS USED FOR BUILDING, IMPLEMENTING, AND VALIDATING THE SM DOWNSCALING ALGORITHM

Data Name	Time Period	Variables	Spatial Resolution	Temporal Resolution
NLDAS	1981-2018	SM/LST	12.5-km	Hourly
LTDR AVHRR	1981-2018	NDVI	5-km	Daily
VIIRS	2018-2019	LST/LAI	400-m	Daily/Biweekly
Aqua MODIS	2018-2019	LST/NDVI	1-km	Daily/Biweekly
SMAP	2018-2019	SM	9-km	Daily
GPM IMERG	2018-2019	Precipitation	10-km	Daily
ISMN	2018-2019	SM	-	Daily

T_B observations through the SCA [1]. The SMAP SM retrievals were produced at a native spatial resolution of ~ 33 – 40 -km and represent SM of top 0–5 cm soil layer when the vegetation water content ≤ 5 kg/m² [17]. In this article, the enhanced level-2 half orbit 9-km SM product (SPL2SMP_E)¹ for implementing the downscaling model. This product applies Gilbert optimal interpolation technique to integrate the antenna temperature data and the SMAP Level 1B T_B data, and generate SM retrievals in 9 km equal area scalable earth grid [19].

B. North America Land Data Assimilation System (NLDAS)

The NLDAS is a system which is composed of LSM datasets from best available observations and harmonized by controlling data quality and spatial/temporal consistency. The NLDAS-2 data is at an hourly temporal interval and a 12.5-km spatial resolution and covers the time period from January 1979 to present. In this study, the Noah LSM level-4 variables: surface skin temperature and SM of 0–10 cm depth soil layer² and used to construct the downscaling model. The NLDAS Noah model was developed as a land component of the National Centers for Environmental Prediction (NCEP) mesoscale Eta model. The previous studies validated and discussed the accuracy of the NLDAS Noah model data, including [72]–[76].

C. Moderate Resolution Imaging Spectroradiometer

The MODIS is an important instrument onboard NASA's satellites Terra (launched in 1999) and Aqua (launched in 2002). It acquires earth's land surface observations from 36 spectral bands in a global coverage and a 1-2 day revisit, and its resolutions range in 250 m–1 km [77]–[79]. In this article, the Aqua MODIS products: 1-km daily LST (MYD11A1) and 1-km biweekly NDVI (MYD13A2)³ for producing the 1-km downscaled SM.

D. Long Term Data Record

The LTDR contains several data sets such as global surface climate data record, including NOAA satellites

N07~N19 advanced very high resolution radiometer (AVHRR) (AVH13C1) and Terra/Aqua MODIS and the time period from 1981-present [80]. A previous study showed that the NDVI derived from MODIS and AVHRR had a high overall correlation of 0.87, which implied that the MODIS NDVI can be used as a continuation of AVHRR NDVI historical data [81]. The LTDR NDVI is a daily gridded data set at 0.05° resolution climate modeling grid. In this article, the AVHRR/MODIS NDVI data of LTDR version 4,⁴ and were upscaled to 12.5-km which is same as the resolution of NLDAS θ and ΔT_s grids.

E. Visible Infrared Imaging Radiometer Suite

The VIIRS instrument is onboard the Suomi NPP satellite, which was launched in 2011, and it has 22 visible and infrared bands for producing global monitoring observations [82]. The VIIRS products include many environmental variables, such as vegetation, fire, snow and ice, clouds and aerosols. The VIIRS is considered as an improvement of the measurements by several previous satellite sensors: AVHRR and MODIS, in terms of providing higher spatial resolution and better accurate observations. In this study, the VIIRS derived LST and LAI products at 400-m resolution were used to implement the downscaling model. The LST were retrieved using the 375-m resolution I5 band (10.5–12.4 μm) by the VIIRS land surface temperature and emissivity algorithm and a single channel atmospheric correction model, and the LAI were retrieved by the MODIS LAI/FPAR operational algorithm, [83]–[85]. The atmospheric profiles (temperature and moisture) needed by the atmospheric correction were from the climate forecast system reanalysis [86].

F. Global Precipitation Mission (GPM)

The GPM is an international satellite mission developed for providing rain and snowfall observations of a new standard. The satellite was launched in February 2014 and it has two instruments onboard: dual-frequency precipitation radar and GPM microwave imager as an extension of the measurement range of the tropical rainfall measuring mission [87]–[88]. We used the Integrated multisatellite retrievals for GPM (IMERG) precipitation data⁵ to compare with SMAP SM time series for evaluating the impact of precipitation.

¹Online. [Available]: https://nsidc.org/data/SPL2SMP_E

²Online. [Available]: <http://ldas.gsfc.nasa.gov/nldas/>

³Online. [Available]: <https://lpdaac.usgs.gov/>

⁴Online. [Available]: <https://ltdr.nascom.nasa.gov/>

⁵Online. [Available]: <https://pmm.nasa.gov/data-access/downloads/gpm>

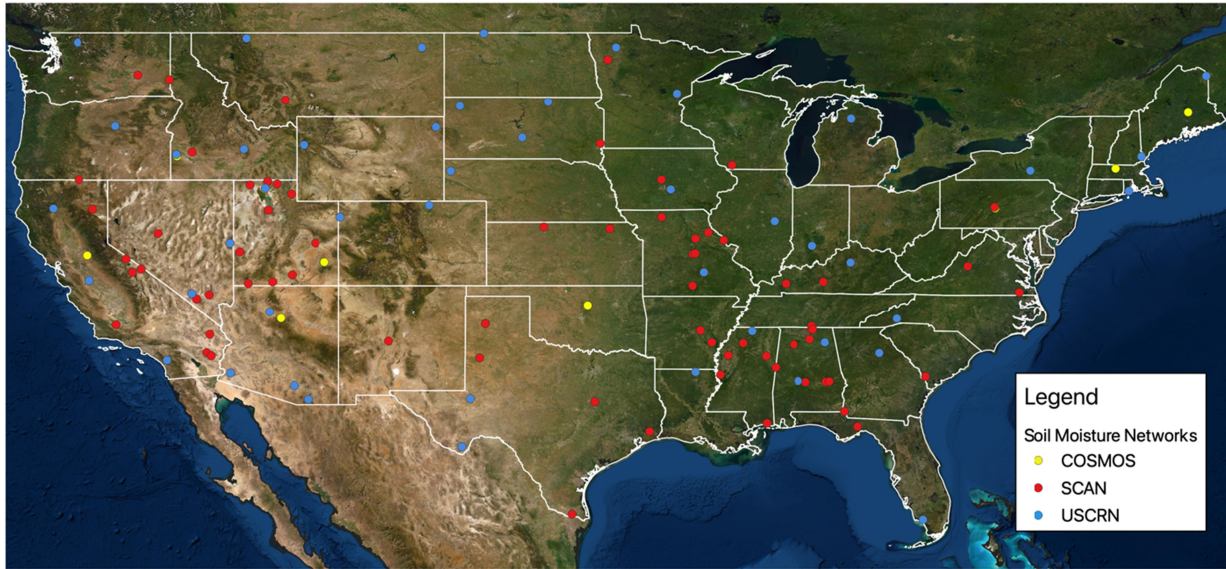


Fig. 1. Map of locations for the 125 SM ground stations from 3 networks acquired from the ISMN website, including COSMOS, SCAN, and USCRN.

G. International Soil Moisture Network (ISMN)

The ISMN is developed for calibrating and validating the data accuracy of remote sensing SM retrievals, as well as improving the performance of SM retrieval algorithms. The ISMN website: <https://ismn.geo.tuwien.ac.at/> provides a global covered repository of *in situ* SM ground measurements from more than 1400 stations of 35 international SM networks, since 1952 [89]–[91]. There have been numerous publications focused on evaluating and discussing the data quality of SM networks by ISMN [92]–[97].

In this article, we selected 125 SM ground stations from three SM networks in the CONUS for validating the downscaled SM data from 2018 to 2019. These stations were selected with the criteria of relatively complete records of *in situ* SM measurements along the time scale, and they cover regions of different climate zones, soil and vegetation types, which are useful for studying their impacts on SM data accuracy. Fig. 1 shows locations of the SM stations. The corresponding SM networks include: cosmic-ray soil moisture observation system (COSMOS), soil climate analysis network (SCAN), and U.S. climate reference network (USCRN). The specifications of the three SM networks are given in Table II(a). Table 2(b) shows the names, SM networks and land cover types of the SM stations. It can be summarized that the SM stations are covered by grassland, mixed leaf type forest, scrubland, cropland, or bare areas.

IV. RESULTS AND DISCUSSION

A. Interpretation of SMAP SM Maps

Fig. 2 compares the downscaled 400-m/1-km SMAP SM with the 9-km SMAP SM from August 1–16, 2019 in the CONUS. It can be summarized that the spatial pattern of the 400-m/1-km SM was consistent with the 9-km SM, but showed more SM spatial features. It is also observed that the 400-m/1-km products had missing data, especially in south central, southeastern

and northeastern CONUS. It is mainly due to the cloud cover issue caused absence of surface temperature retrievals from VIIRS/MODIS. Another reason is we discarded the pixels of LST retrievals which are labeled as missing or poorly/badly calibrated, by the associated data quality flag of VIIRS/MODIS data.

As a case study, Fig. 3(a)–(b) shows the comparisons between the 400-m, 1-km, and 9-km SMAP SM at the watershed scale: middle Snake river basin (MSRB) and upper Washita river basin (UWRB) from August 1–24, 2019. From Fig. 3(a), the Snake river and floodplains along the river channel can be clearly observed only at the 400-m maps. In the northwestern MSRB, a SM wetting trend with high spatial heterogeneity can be noted at the 400-m/1-km maps, in the areas dominated by crop fields. Additionally, from the 400-m/1-km maps, a region with high SM values could be found along the south central edges of MSRB. This region corresponds to high-elevation coniferous forests where the SM wetting trend is observed. None of the abovementioned features is found in the 9-km maps. On the other hand, in Fig. 3(b), the 400-m/1-km SM show a wetting trend from August 9–16 and then a dry-down trend from August 17–24, with greater spatial/temporal variability than 9-km SM. The entire UWRB has a complex landcover of mixed cropland, forest and grassland and the easternmost UWRB has a larger proportion of forests than the western part. The landcover induced SM spatial pattern features are reflected on the SM maps: The 400-m SM maps generally show greater SM spatial heterogeneity than the 1-km/9-km maps. From the 400-m maps, the easternmost UWRB demonstrates a SM wetting trend in detail in time series, which is not reflected on either 1-km or 9-km maps.

B. Analyses of Validation Results

The statistical variables: R^2 , unbiased RMSE (ubRMSE), bias b , and relative difference p were calculated to validate

TABLE II
(A) SPECIFICATIONS OF SM NETWORKS ACQUIRED FROM THE ISMN WEBSITE USED FOR VALIDATION

Network	Measuring Device	Number of Stations
COSMOS	Cosmic ray probe	10
SCAN	Hydraprobe	69
USCRN	Hydraprobe	46

(b) NAMES, SM NETWORKS AND LAND COVER TYPES OF THE SM STATIONS ACQUIRED FROM ISMN.

Site Name	Network	Land Cover Types	Site Name	Network	Land Cover Types
Bushland	COSMOS	Grassland	Stanley Farm	SCAN	Mosaic tree and shrub/herbaceous cover
Flag Ponderosa Pine	COSMOS	Tree cover, needle-leaved, evergreen	Starkville	SCAN	Grassland
Harvard Forest	COSMOS	Tree cover, broadleaved, deciduous	Sudduth Farms	SCAN	Tree cover, mixed leaf type (broadleaved and needle-leaved)
Howland	COSMOS	Tree cover, needle-leaved, evergreen	Table Mountain	SCAN	Grassland
Lower Salt Creek	COSMOS	Shrubland	Tnc Fort Bayou	SCAN	Mosaic natural vegetation (tree, shrub, herbaceous cover) / cropland
Reynolds Creek	COSMOS	Shrubland	Tidewater Arec	SCAN	Cropland, rainfed
SMAP-OK	COSMOS	Grassland	Trough Springs	SCAN	Grassland
Shale Hills	COSMOS	Tree cover, broadleaved, deciduous	Tuskegee	SCAN	Tree cover, needle-leaved, evergreen
Tonzi Ranch	COSMOS	Grassland	UAPB Dewitt	SCAN	Cropland, rainfed
Tower Ruin	COSMOS	Shrubland	UAPB Lonoke Farm	SCAN	Cropland, rainfed
Ames	SCAN	Cropland, rainfed	UW Platteville	SCAN	Cropland, rainfed
Beaumont	SCAN	Cropland, rainfed / Herbaceous cover	Vermillion	SCAN	Tree cover, needle-leaved, evergreen
Blue Creek	SCAN	Grassland	WTARS	SCAN	Grassland
Bodie Hills	SCAN	Shrubland	Wakulla #1	SCAN	Tree cover, needle-leaved, evergreen
Bragg Farm	SCAN	Cropland, rainfed	Weslaco	SCAN	Cropland, rainfed
Busby Farm	SCAN	Grassland	Youmans Farm	SCAN	Mosaic natural vegetation (tree, shrub, herbaceous cover)/ cropland
Bushland #1	SCAN	Grassland	Aberdeen 35 WNW	USCRN	Grassland
CMRB LTAR-MO	SCAN	Cropland, rainfed	Arco 17 SW	USCRN	Tree cover, needle-leaved, evergreen
Cache Junction	SCAN	Cropland, rainfed	Asheville 13 S	USCRN	Grassland
Carver Farm	SCAN	Grassland	Baker 5 W	USCRN	Shrubland
Centralia Lake	SCAN	Grassland	Bedford 5 WNW	USCRN	Grassland
Chicken Ridge	SCAN	Grassland	Brigham City 28 WNW	USCRN	Shrubland
Cochora Ranch	SCAN	Shrubland	Buffalo 13 ESE	USCRN	Grassland
Cook Farm	SCAN	Cropland, rainfed	Champaign 9 SW	USCRN	Cropland, rainfed
Field D	SCAN	Cropland, rainfed			

the accuracy of the original 9-km and downscaled SMAP SM products at 400 m/1 km, as shown

$$R^2 = 1 - \frac{\sum (\theta_i - \hat{\theta}_i)^2}{\sum (\theta_i - \bar{\theta})^2} \quad (3)$$

$$\text{ubRMSE} = \sqrt{\frac{\sum_{i=1}^n (\theta_i - (\hat{\theta}_i - b))^2}{n}} \quad (4)$$

$$b = \frac{\sum_{i=1}^n (\theta_i - \hat{\theta}_i)}{n} \quad (5)$$

TABLE II (B)
 NAMES, SM NETWORKS, AND LAND COVER TYPES OF THE SM STATIONS ACQUIRED FROM ISMN

Dee River Ranch	SCAN	Cropland, rainfed / Herbaceous cover	Darrington 21 NNE	USCRN	Tree cover, needle-leaved, evergreen
Desert Center	SCAN	Shrubland	Des Moines 17 E	USCRN	Cropland, rainfed
Doe Ridge	SCAN	Shrubland	Dinosaur 2 E	USCRN	Shrubland
Eagle Lake	SCAN	Tree cover, needle-leaved, evergreen	Durham 2 SSW	USCRN	Tree cover, broadleaved, deciduous
Elsberry Pmc	SCAN	Grassland	Elgin 5 S	USCRN	Shrubland
Eros Data Center	SCAN	Cropland, rainfed	Everglades City 5 NE	USCRN	Shrub or herbaceous cover, flooded, fresh/saline/brakish water
Essex	SCAN	Shrubland	Fallbrook 5 NE	USCRN	Tree cover, needle-leaved, evergreen
Ford Dry Lake	SCAN	Bare areas	Gadsden 19 N	USCRN	Grassland
Glacial Ridge	SCAN	Cropland, rainfed	Gaylord 9 SSW	USCRN	Mosaic cropland/ natural vegetation (tree, shrub, herbaceous)
Goodwin Creek Pasture	SCAN	Mosaic tree and shrub (>50%) / herbaceous cover (<50%)	Goodridge 12 NNW	USCRN	Cropland, rainfed
Grantsville	SCAN	Shrubland	Harrison 20 SSE	USCRN	Grassland
Green River	SCAN	Cropland, rainfed	Holly Springs 4 N	USCRN	Mosaic natural vegetation (tree, shrub, herbaceous cover)/ cropland
Hals Canyon	SCAN	Shrubland	Ithaca 13 E	USCRN	Cropland, rainfed
Journagan Ranch	SCAN	Grassland	John Day 35 WNW	USCRN	Shrubland
Levelland	SCAN	Cropland, rainfed	Kingston 1 W	USCRN	Cropland, rainfed
Lind #1	SCAN	Cropland, rainfed	Limestone 4 NNW	USCRN	Mosaic tree and shrub/ herbaceous cover
Lynhart Ranch	SCAN	Cropland, rainfed	Merced 23 WSW	USCRN	Grassland
Mammoth Cave	SCAN	Tree cover, broadleaved, deciduous	Mercury 3 SSW	USCRN	Shrubland
Marble Creek	SCAN	Shrubland	Monahans 6 ENE	USCRN	Shrubland
Mark Twain HS	SCAN	Cropland, rainfed	Monroe 26 N	USCRN	Tree cover, needle-leaved, evergreen
Mcalister Farm	SCAN	Cropland, rainfed	Moose 1 NNE	USCRN	Tree cover, needle-leaved, evergreen
Morris Farms	SCAN	Mosaic natural vegetation	Murphy 10 W	USCRN	Grassland
Onward	SCAN	Cropland, rainfed	Northgate 5 ESE	USCRN	Grassland
Orchard Range Site	SCAN	Shrubland	Nunn 7 NNE	USCRN	Grassland
Park Valley	SCAN	Grassland	Panther Junction 2 N	USCRN	Shrubland
Phillipsburg	SCAN	Grassland	Pierre 24 S	USCRN	Grassland
Pine Nut	SCAN	Grassland	Redding 12 WNW	USCRN	Tree cover, needle-leaved, evergreen
Porter Canyon	SCAN	Shrubland	Salem 10 W	USCRN	Grassland
Princeton #1	SCAN	Cropland, rainfed	Sandstone 6 W	USCRN	Tree cover, broadleaved, deciduous
Riesel	SCAN	Grassland	Selma 13 WNW	USCRN	Grassland
River Road Farms	SCAN	Cropland, rainfed	St. Mary 1 SSW	USCRN	Urban areas
Rock Springs PA	SCAN	Cropland, rainfed	Sundance 8 NNW	USCRN	Tree cover, needle-leaved, evergreen
Sand Hollow	SCAN	Grassland	Tucson 11 W	USCRN	Shrubland
Sandy Ridge	SCAN	Cropland, rainfed	Versailles 3 NNW	USCRN	Grassland
Selma	SCAN	Tree cover, needle-leaved, evergreen	Watkinsville 5 SSE	USCRN	Grassland
Sevilleta	SCAN	Grassland	Williams 35 NNW	USCRN	Shrubland
Shenandoah	SCAN	Tree cover, broadleaved, deciduous	Wolf Point 29 ENE	USCRN	Grassland
Spickard	SCAN	Grassland	Yuma 27 ENE	USCRN	Shrubland
Spooky	SCAN	Grassland			

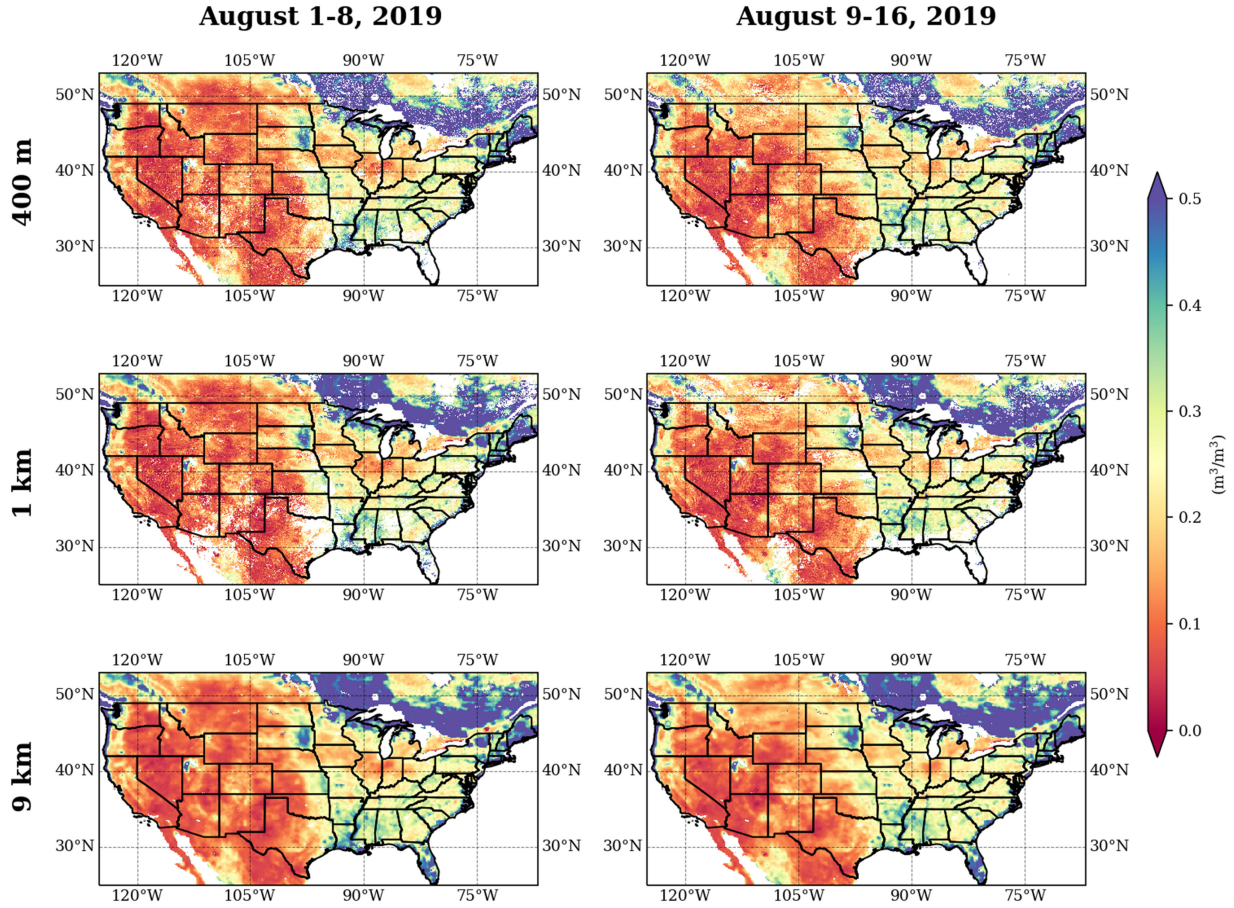


Fig. 2. Comparisons of 8-day SMAP SM composites between the 400-m from the improved downscaling algorithm, 1 and 9 km in the CONUS from August 1–16, 2019

$$p = 100\% \times (u_{\theta} - u_{\hat{\theta}}) / u_{\theta} \quad (6)$$

Where θ is in situ SM and $\hat{\theta}$ is the three SMAP SM data at 400-m, 1-km and 9-km resolutions. ubRMSE is the unbiased RMSE by removing the bias b from $\hat{\theta}$. p is the relative difference of ubRMSE in percent between the original 9-km SM (u_{θ}) and downscaled SM ($u_{\hat{\theta}}$) at 400-m/1-km resolutions.

Fig. 4 shows validation metrics R^2 and RMSE of the 400-m SMAP SM from the improved downscaling algorithm, corresponding to the 125 in situ stations in the CONUS. We find that many in situ stations with relatively high R^2 values (>0.6) presented in northwestern and southeastern regions of CONUS. On the other hand, nearly ten stations with high RMSE values ($>0.15 \text{ m}^3/\text{m}^3$) can also be observed in southeastern CONUS (Alabama, Georgia and Florida). It can be inferred that the abovementioned stations have low variance but high bias correlations with *in situ* SM. Besides, there are a few stations in the Rocky mountain regions: Northern California, Utah, Colorado, as well as New England region that have high RMSEs ($>0.15 \text{ m}^3/\text{m}^3$). The RMSEs for the rest of stations in the CONUS are generally less than $0.15 \text{ m}^3/\text{m}^3$.

Fig. 5 is the Taylor diagram of three validation metrics of the 400-m SMAP SM from the improved downscaling algorithm at the 125 *in situ* stations in the CONUS. We can summarize that, for the correlation coefficient (R), a large proportion of stations

fall within the range of 0.2–0.9. However, it is observed that a few stations have low σ ($<0.025 \text{ m}^3/\text{m}^3$) but low R (<0.2). On the other side, standard deviation (SD) and root-mean-square deviation (RMSD) for approximately 90% of the stations are less than 0.09 and $0.06 \text{ m}^3/\text{m}^3$, respectively. The overall RMSD range is close to the baseline requirement for SMAP SM ($0.04 \text{ m}^3/\text{m}^3$), which implies an overall moderate good accuracy for most of the stations.

Table III gives the validation results of the 400-m SM from the improved and original downscaling algorithms, 1-km and 9-km SMAP SM by SM network, while Fig. 6 shows the site-specific validation scatterplots of the three SM networks. From Table III, it can be summarized that ubRMSE for the 400-m SM of the improved/original algorithms (0.068 – $0.08 \text{ m}^3/\text{m}^3$ and 0.07 – $0.083 \text{ m}^3/\text{m}^3$, respectively) and 1-km SM (0.07 – $0.081 \text{ m}^3/\text{m}^3$) all have an improvement over the 9-km SM (0.076 – $0.09 \text{ m}^3/\text{m}^3$) for all three SM networks, while bias for the 400-m SM of the improved/original algorithms (0.01 and 0.055 – $0.072 \text{ m}^3/\text{m}^3$, respectively) and 1-km SM (0.053 – $0.071 \text{ m}^3/\text{m}^3$) all decrease from the 9-km SM (range 0.06 – $0.08 \text{ m}^3/\text{m}^3$). The ubRMSEs decrease on average by 0.01 or 12.8% for the 400-m SM of the improved algorithm, and decrease on average by $0.007 \text{ m}^3/\text{m}^3$ or 8.7% for the 400-m of the original algorithm, and decrease on average by $0.012 \text{ m}^3/\text{m}^3$ or 16% for the 1-km SM, respectively, from the 9-km SM. It is also found that the ubRMSE and bias

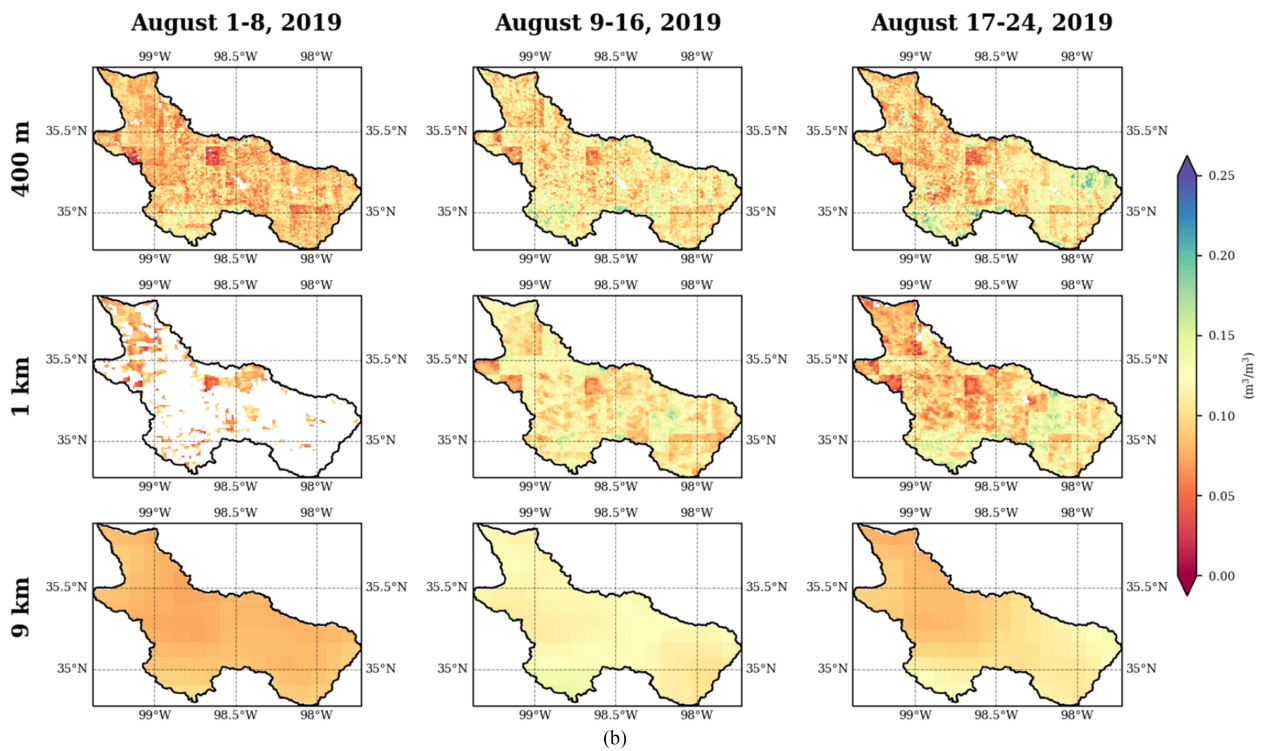
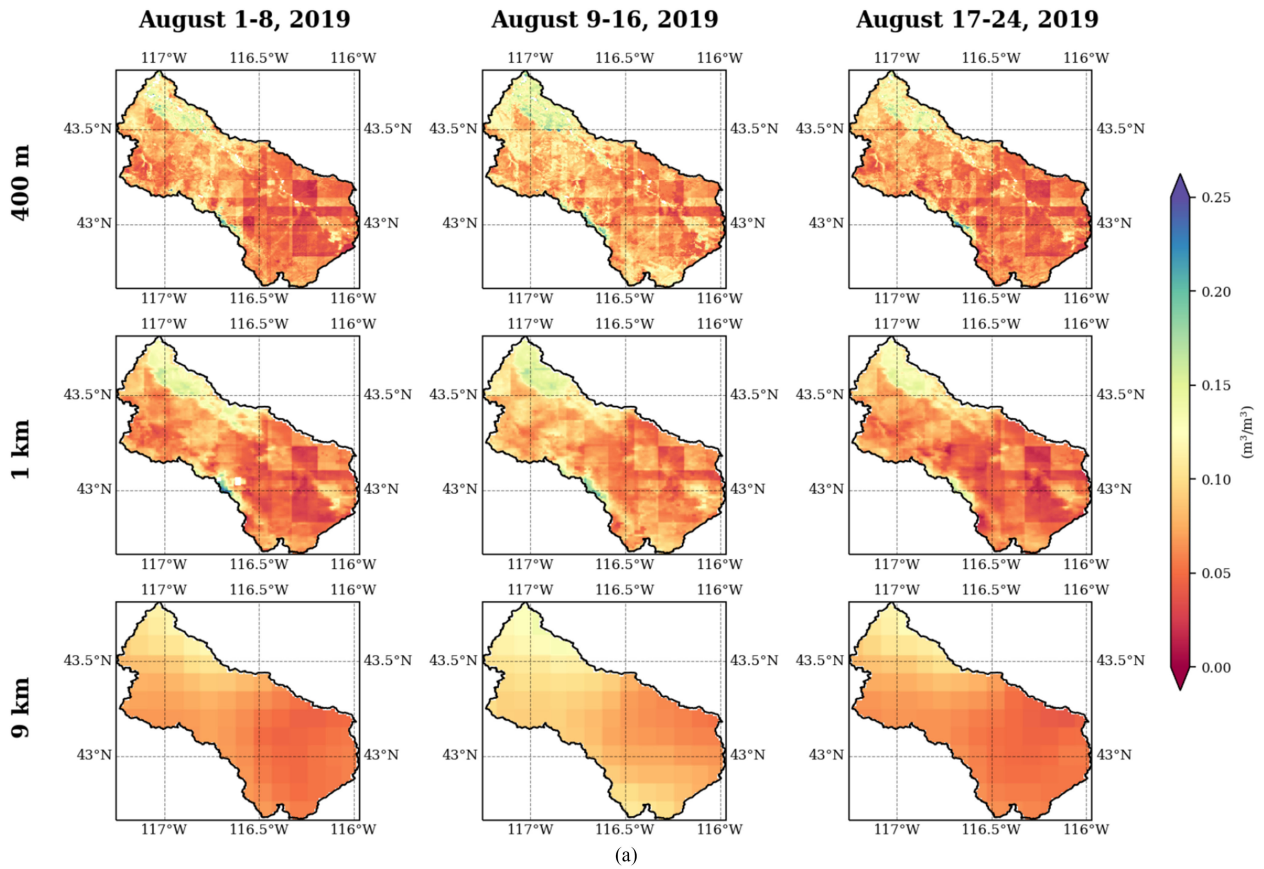


Fig. 3. Comparisons of eight-day SMAP SM composites between the 400 m from the improved downscaling algorithm, 1 km and 9 km in (a) middle Snake river basin and (b) upper Washita river basin from August 1–24, 2019.

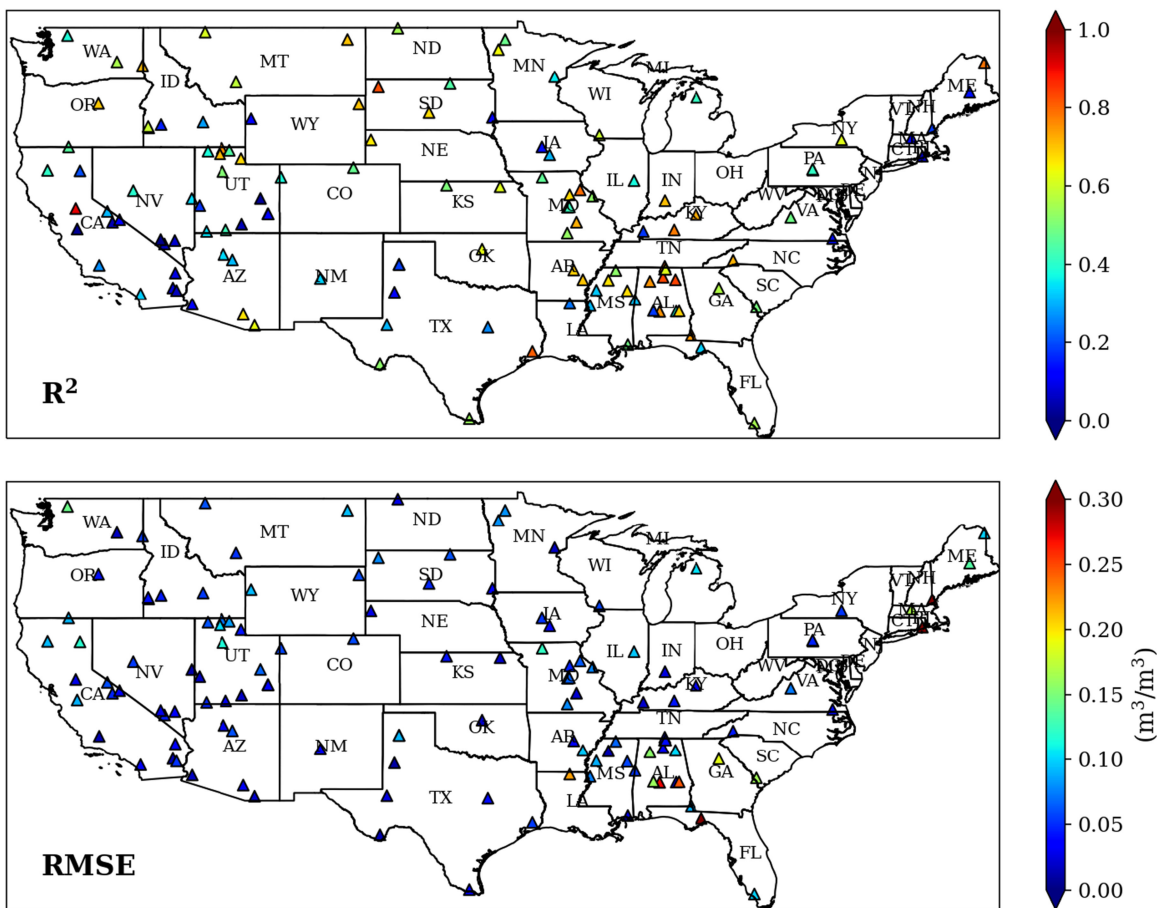


Fig. 4. Maps show R^2 and RMSE corresponding to the 125 ISMN *in situ* stations in the CONUS for validating the 400-m SMAP SM from the improved downscaling algorithm. The validation data are from three SM networks: COSMOS; SCAN; and USCRN, from 2018 to 2019.

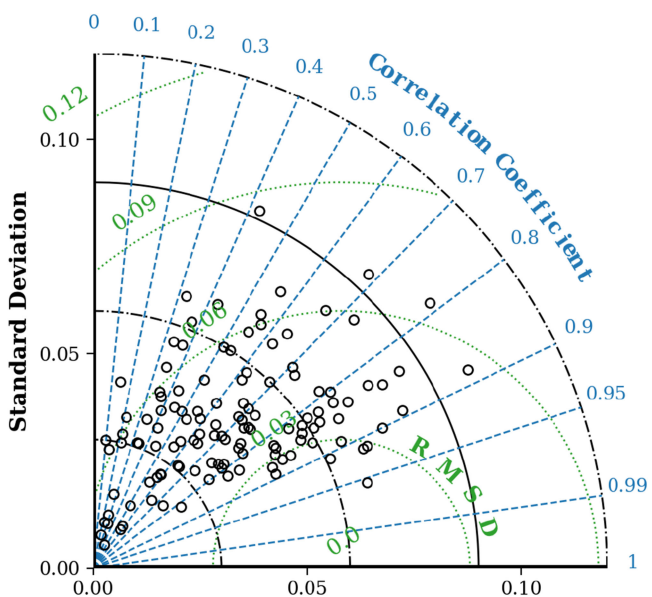


Fig. 5. Taylor diagram shows three validation variables: correlation coefficient, RMSD, and SD for the 400-m SMAP SM from the improved downscaling algorithm, using *in situ* measurements from three SM networks: COSMOS, SCAN and USCRN from 2018 to 2019.

for the 400-m SM of the improved algorithm are generally lower than either the 400-m SM of the original algorithm or the 1-km SM in SCAN and USCRN. On the other hand, R^2 for the 400-m SM (0.343–0.474 and 0.35–0.487, respectively) of the improved/original algorithms and 1-km SM (0.339–0.494) are lower than at 9-km SM (0.422–0.51), which do not show improvement. This result is mainly due to the high bias and low variance tradeoff issue. More specifically, one 9-km grid value may correspond to more *in situ* measurements within its boundaries than either the 400-m or 1-km. Consequently, the 9-km SM validation point-pairs show less variances, but higher biases than either the 400-m or 1-km SM point-pairs, which means the 9-km point-pairs are higher concentrated but also higher systematically biased. For instance, this issue can be noted from several sites in Fig. 6: Flag Ponderosa Pine; Grantsville; and Sandstone 6W. If we compare between different SM networks, for the validation results of the 400-m SM from the improved algorithms, USCRN has relatively higher R^2 (0.474), but also higher ubRMSE and bias (0.08 and 0.07 m^3/m^3 , respectively) than the other two networks. From Fig. 6, it can be known that the regression fit lines for the 400-m/1-km SM are closer to the 1-1 line than for the 9-km SM from all three networks. The point pairs of the 9-km SM are more concentrated than either

TABLE III
 STATISTICAL METRICS BY USING ISMN SM MEASUREMENTS FROM THREE SM NETWORKS FOR VALIDATING THE 400-m FROM THE ORIGINAL/IMPROVED DOWNSCALING ALGORITHMS, 1-KM AND 9-KM SMAP SM DATA

400-m (improved)				
Network	Number of Points	R ²	ubRMSE	bias
COSMOS	207	0.343	0.078	0.066
SCAN	2439	0.43	0.068	0.052
USCRN	1696	0.474	0.08	0.07
400-m				
COSMOS	207	0.35	0.083	0.072
SCAN	2439	0.425	0.07	0.055
USCRN	1696	0.487	0.082	0.072
1-km				
COSMOS	207	0.339	0.07	0.053
SCAN	2439	0.467	0.07	0.054
USCRN	1696	0.494	0.081	0.071
9-km				
COSMOS	207	0.422	0.09	0.077
SCAN	2439	0.465	0.076	0.06
USCRN	1696	0.51	0.089	0.08

the 400-m or 1-km SM, however, they also demonstrate a greater systematically biased trend than the other two SM products.

Table IV gives the summarized validation results which were classified into six geographic regions by *in situ* station coordinates, based on the simplified U.S. climate region classification system [98]. Similarly, both 400-m and 1-km validation results have lower ubRMSE and bias than 9-km for all 6 regions, while R² of only 2 regions (the north east and south east) are improved. Specifically, ubRMSEs are improved on average by 0.008 m³/m³ or 12.7% for the 400-m SM of the improved algorithm, and improved on average by 0.006 m³/m³ or 9.1% for the 400-m SM of the original algorithm, and improved by 0.008 m³/m³ or 11.3% for the 1-km SM, from the 9-km SM. With respect to the geographical regions, the north /south central, northwest, and southwest regions have a greater improvement of ubRMSE or bias than the northeast and southeast regions for all 3 SM data sets. For example, ubRMSE and bias for the 400-m SM of the improved algorithm in the north /south central regions (0.056–0.062 m³/m³ and 0.043–0.044 m³/m³, respectively), or the northwest/southwest regions (0.048–0.057 m³/m³ and 0.038 m³/m³, respectively) are generally 0.05–0.06 m³/m³ lower than the northeast/southeast regions (0.111–0.113 m³/m³ and 0.1–0.102 m³/m³, respectively). On the other hand, ubRMSE and bias for the 400-m SM of the improved algorithm (range 0.048–0.113 m³/m³ and 0.038–0.102 m³/m³, respectively) are

overall lower than the metrics for the 400-m SM of the improved algorithm (range 0.052–0.117 m³/m³ and 0.042–0.103 m³/m³, respectively), which indicates the better accuracy of the improvement algorithm. And, ubRMSE and bias for the 400-m SM of the improved algorithm outperform the metrics for the 1-km SM (range 0.049–0.115 m³/m³ and 0.036–0.107 m³/m³, respectively) in four regions: North/South Central, South East and South West.

Fig. 7 shows time series analyses of the 400-m from the improved and original downscaling algorithms, 1-km and 9-km SMAP SM comparing with *in situ* measurements and GPM precipitation corresponding to the three networks on April–September of 2018 and 2019. It can be summarized that the 400-m/1-km SM had a better agreement with *in situ* data than 9-km. Furthermore, for the stations located in arid/semi-arid regions where have low precipitation, such as Tonzi Ranch (COSMOS), Lind #1 (SCAN) and Tucson 11W (USCRN), a good agreement between the three SMAP SM data sets and *in situ* data can be noticed. As opposed to this, inconsistency can be observed between all three SMAP SM data sets and *in situ* SM during rainy days. This is possibly due to the negative impacts of precipitation and cloud cover on data quality of the 9-km SMAP SM and MODIS/VIIRS LST products. Additionally, precipitation generally occurred at a larger scale than the downscaled SM data pixel size (400-m or 1-km). Therefore,

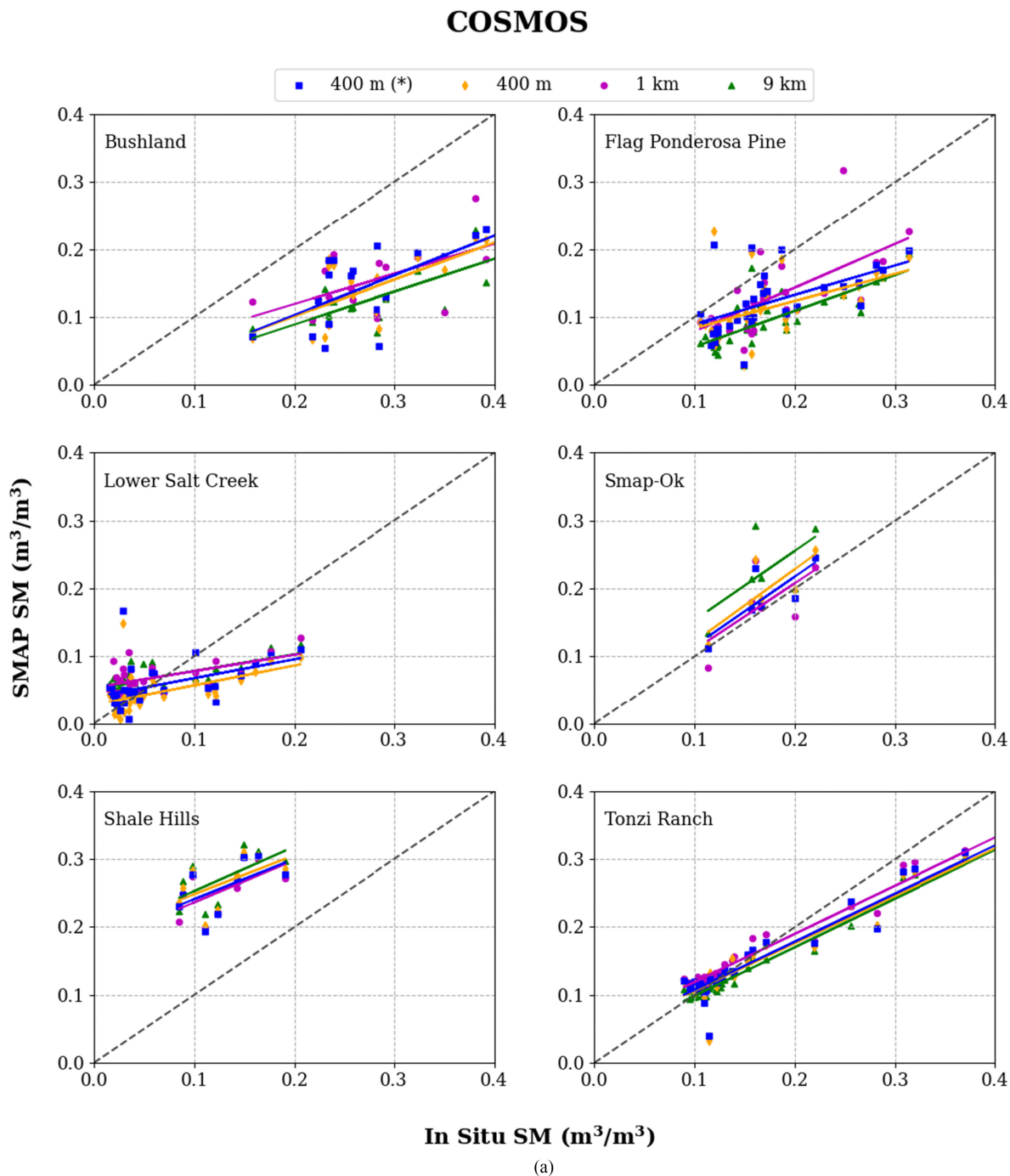


Fig. 6. Validation scatterplots between *in situ* SM and the 400 m from the improved (denoted as *) and original downscaling algorithms, 1-km and 9-km SMAP SM in three SM networks: (a) cosmic-ray soil moisture observation system; (b) soil climate analysis network; and (c) U.S. climate reference network, from April to September, 2018–2019.

precipitation cannot be an indicator on the performance of the downscaling algorithm and accuracy of the downscaled SM is not clearly improved over the 9-km SM during rainy days.

V. CONCLUSION

In this article, an improved SM downscaling algorithm which was based on vegetation modulated ATI relationship between

LST difference and surface SM was implemented. The algorithm was utilized to downscale the 9-km SMAP enhanced L2 radiometer half-orbit SM product at 400-m/1-km resolution in the CONUS using VIIRS/MODIS data. A major improvement of the original algorithm was intended to minimize the sharp edge effect caused by the mismatch between SMAP and VIIRS/MODIS boundaries. The performance of the algorithm validated by *in situ* SM measurements shows that the 400-m/1-km downscaled SM display greater SM spatial and temporal

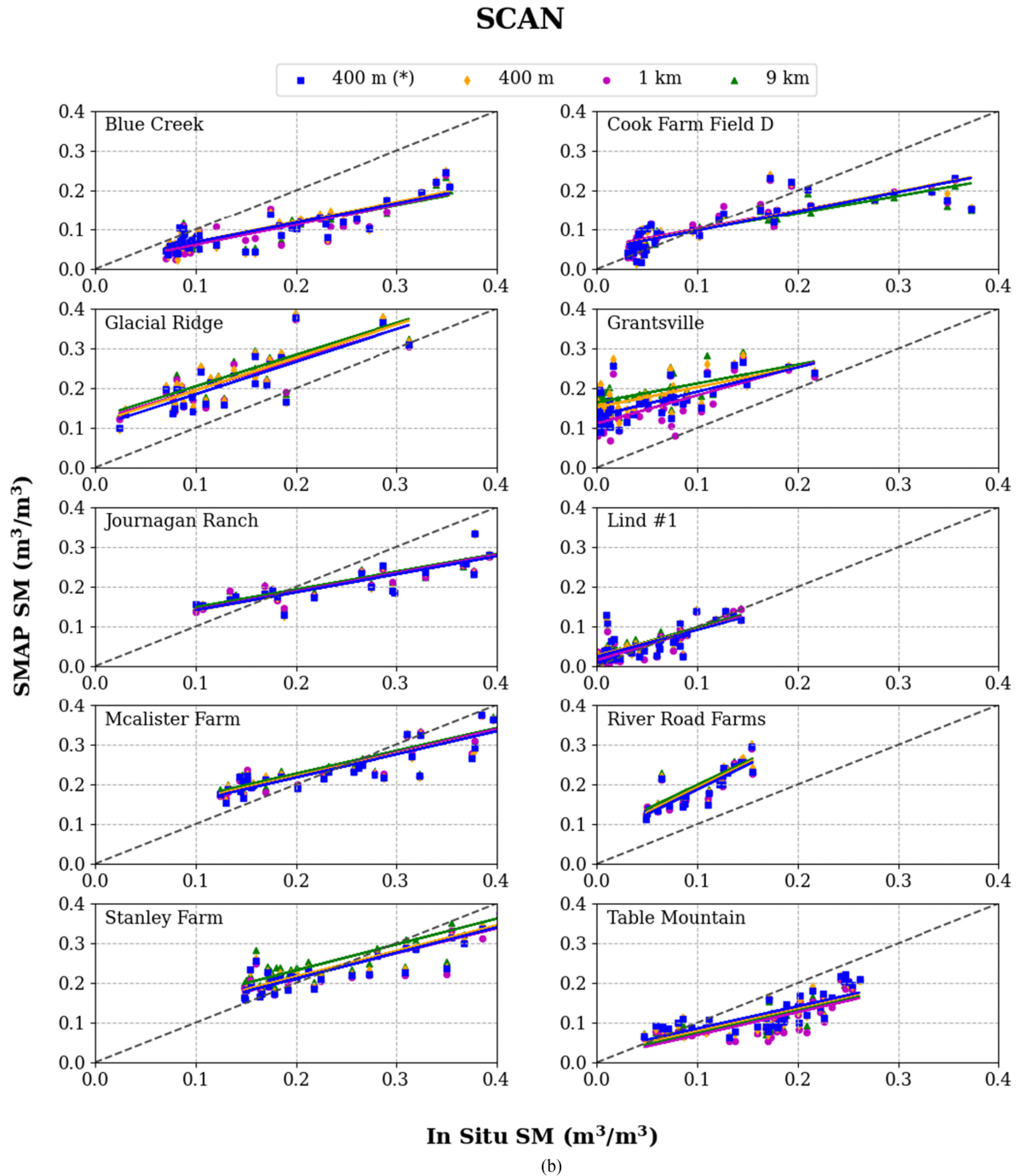


Fig. 6. Continue.

variability on watershed scale. The validation results also show that overall ubRMSE of the 400-m/1-km SM outperform the 9-km SM at three SM networks, with both overall ubRMSE and bias decreased. The 400-m SM of the improved downscaling algorithm have generally lower ubRMSE and bias than either the 400-m of the original downscaling algorithm or the 1-km SM, which indicates better data accuracy of the improved algorithm. The validation results prove that the downscaled SM products not only maintain a good accuracy, but also offer greater SM information than the original SMAP SM product. On the other

hand, the algorithm performs better for the stations located in the central and western CONUS, which correspond to arid/semi-arid regions with low precipitation. The precipitation has an impact on quality of the original 9-km SM data, and the downscaled SM do not show clear improvement over the 9-km SM during rainy days.

It is worth noting that there are limitations of this algorithm, as follows: First, quality of the downscaled SM mostly depends on the original SMAP SM and VIIRS/MODIS data. Studies have shown that more uncertainties and errors enter the SMAP

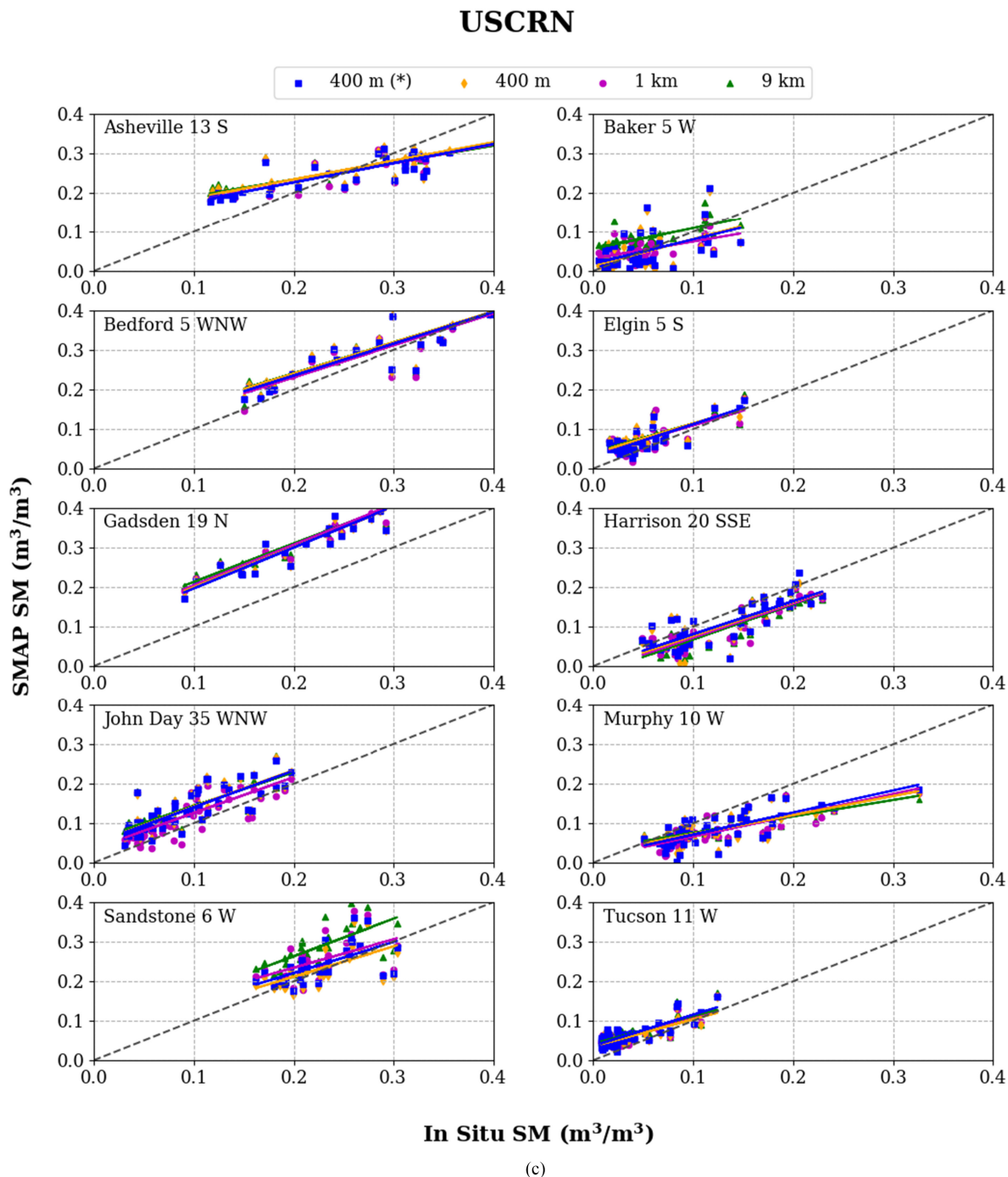


Fig. 6. Continue.

SM retrievals in the regions with greater vegetation or complex topography [18], [99]–[100]. Additionally, the VIIRS/MODIS data are only available for clear sky conditions. The complex terrain and cloud cover issues could cause biased retrievals or data missing [101]. Second, the data sets used in model building and implementation, which include the SM retrievals and LST/vegetation indices, are from different platforms and represent different sensing depths. Finally, in the case of validation, a mismatch exists between the remotely sensed/LSM

area and point scale ground measurements. The microwave SM, VIS/IR and NLDAS data are on a scale of kilometers, compared to in situ SM measurements that are on a point scale [102]–[104].

The downscaled 400-m and 1-km SM represent a big step forward use of satellite derived SM in watershed studies. Specifically, the downscaled 400-m SM represents field-scale SM can be used for smaller watersheds where individual farms need to be characterized for land use changes and/or movement of nutrients, sediments of other pollutants.

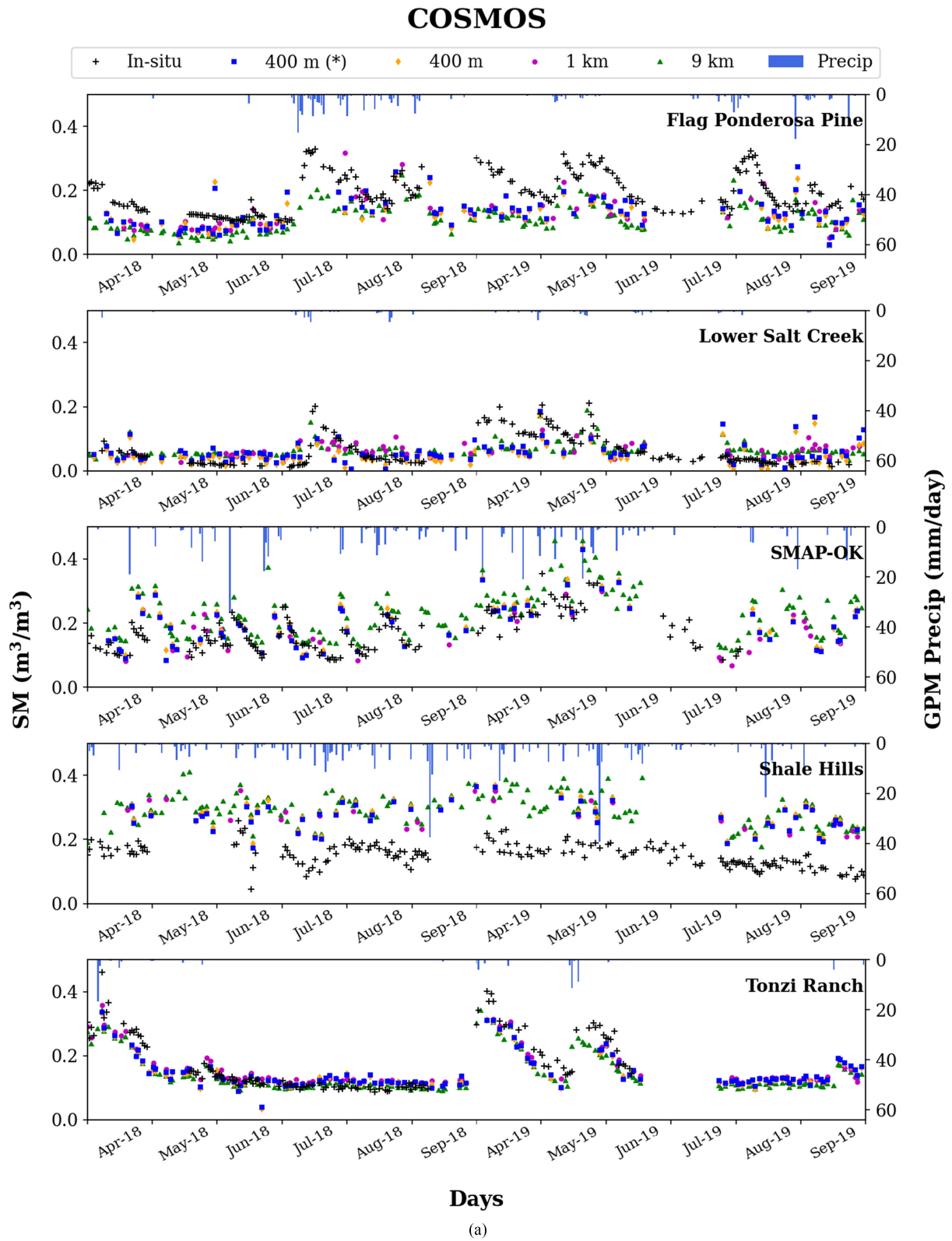


Fig. 7. Time series of *in situ* SM comparing with the 400 -m from the improved (denoted as *) and original downscaling algorithms, 1 and 9 km SMAP SM, as well as the GPM precipitation at 20 stations from three ISMN SM networks: (a) cosmic-ray soil moisture observation system; (b) soil climate analysis network; and (c) U.S. climate reference network, from April to September, 2018–2019.

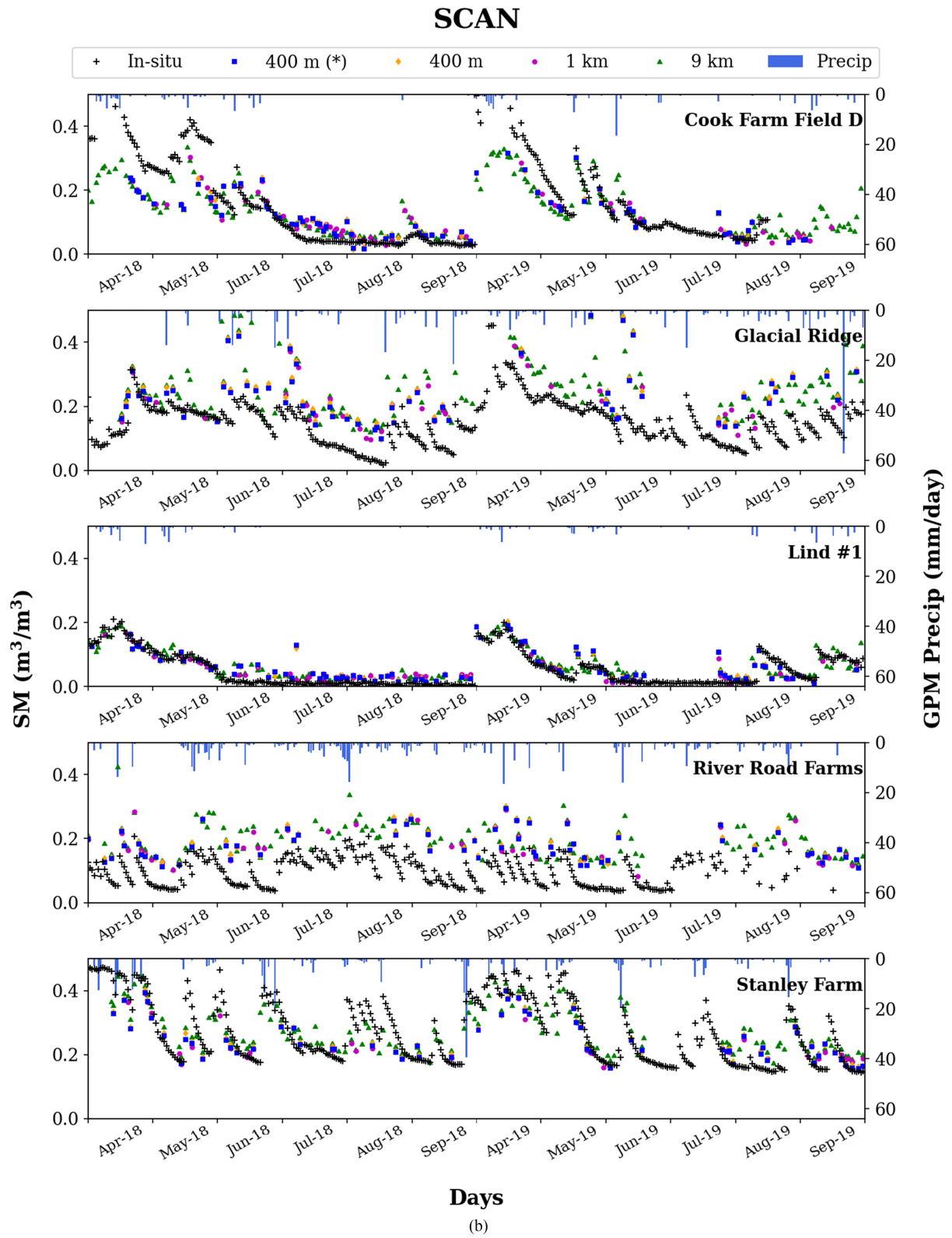


Fig. 7. Continue.

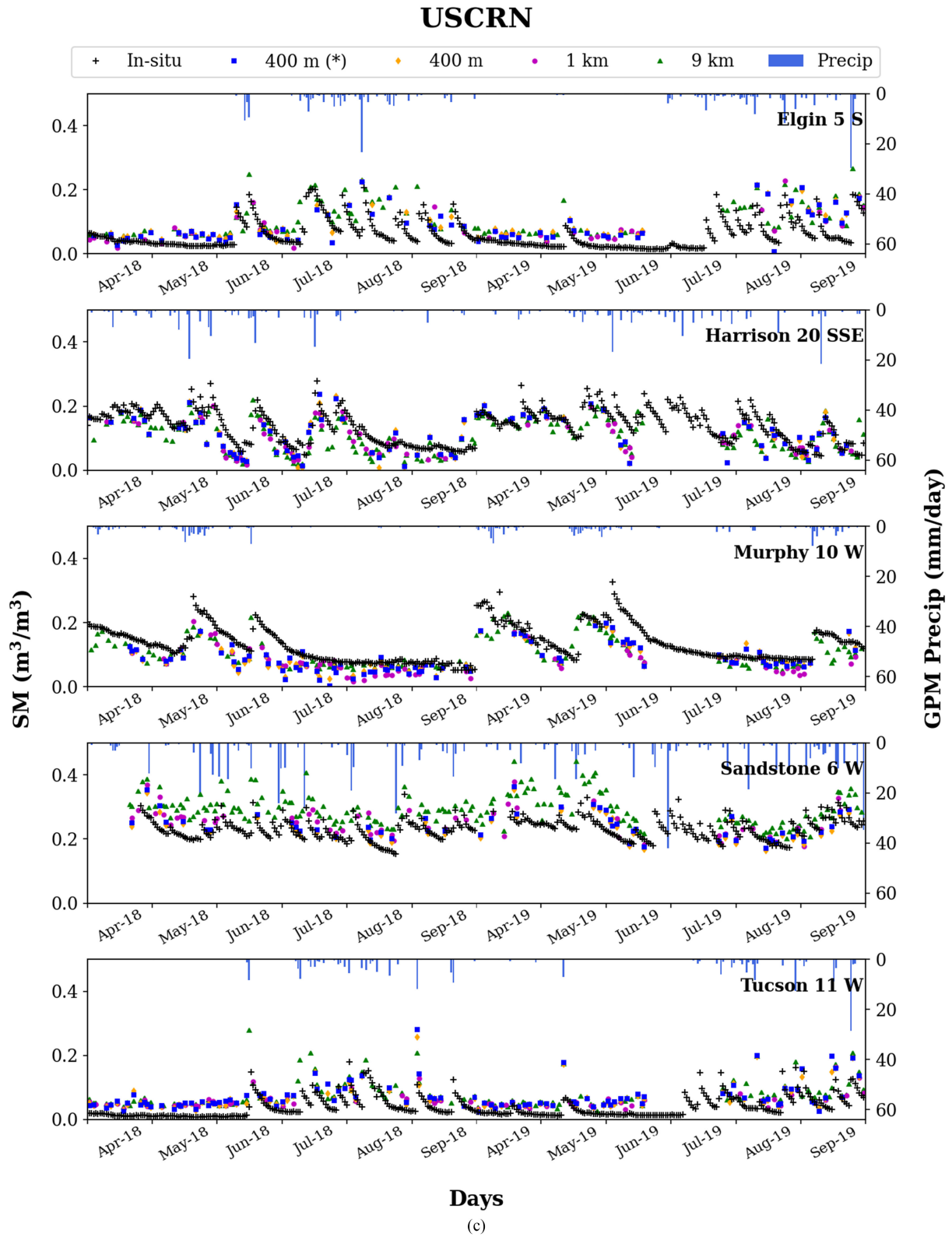


Fig. 7. Continue.

TABLE IV
 STATISTICAL METRICS FOR VALIDATING THE 400 M FROM THE ORIGINAL/IMPROVED DOWNSCALING ALGORITHMS, 1 AND 9-KM SMAP SM DATA USING ISMN SM MEASUREMENTS. THE ISMN STATIONS WERE CLASSIFIED INTO 6 GEOGRAPHIC REGIONS BY STATION COORDINATES

Region	Number of Points	R ²	ubRMSE	bias
400-m (improved)				
North Central	561	0.494	0.056	0.044
North East	356	0.415	0.113	0.1
North West	428	0.455	0.057	0.038
South Central	666	0.505	0.061	0.042
South East	477	0.558	0.111	0.102
South West	1876	0.304	0.048	0.038
400-m				
North Central	561	0.511	0.058	0.045
North East	356	0.403	0.117	0.102
North West	428	0.46	0.059	0.042
South Central	666	0.518	0.065	0.047
South East	477	0.556	0.112	0.103
South West	1876	0.298	0.052	0.042
1-km				
North Central	562	0.49	0.06	0.046
North East	344	0.399	0.112	0.096
North West	428	0.508	0.056	0.036
South Central	666	0.526	0.062	0.042
South East	477	0.576	0.115	0.107
South West	1947	0.369	0.049	0.039
9-km				
North Central	562	0.532	0.066	0.055
North East	344	0.393	0.122	0.107
North West	428	0.517	0.063	0.045
South Central	666	0.555	0.07	0.05
South East	477	0.545	0.12	0.111
South West	1947	0.382	0.06	0.049

ACKNOWLEDGMENT

The authors would like to graciously acknowledge funding from the NASA Terrestrial Hydrology Program (Program Manager Jared Entin) that has supported this work. USDA is an equal opportunity provider and employer. This work was supported in part by the U.S. Department of Agriculture (USDA), Agricultural Research Service.

REFERENCES

- [1] T. J. Jackson, "III. Measuring surface soil moisture using passive microwave remote sensing," *Hydrolog. Processes*, vol. 7, no. 2, pp. 139–152, 1993.
- [2] E. G. Njoku and D. Entekhabi, "Passive microwave remote sensing of soil moisture," *J. Hydrol.*, vol. 184, no. 1/2, pp. 101–129, Oct. 1996.
- [3] V. Lakshmi, J. Fayne, and J. Bolten, "A comparative study of available water in the major river basins of the world," *J. Hydrol.*, vol. 567, pp. 510–532, Dec. 2018.

- [4] V. Lakshmi, E. F. Wood, and B. J. Choudhury, "A soil-canopy-atmosphere model for use in satellite microwave remote sensing," *J. Geophys. Res., Atmos.*, vol. 102, no. D6, pp. 6911–6927, Mar. 1997.
- [5] V. Lakshmi, "The role of satellite remote sensing in the prediction of ungauged basins," *Hydrolog. Processes*, vol. 18, no. 5, pp. 1029–1034, Mar. 2004.
- [6] V. Sridhar, W. T. A. Jaksa, B. Fang, V. Lakshmi, K. G. Hubbard, and X. Jin, "Evaluating bias-corrected AMSR-E soil moisture using in situ observations and model estimates," *Vadose Zone J.*, vol. 12, no. 3, pp. 1–13, Aug. 2013.
- [7] E. G. Njoku, T. J. Jackson, V. Lakshmi, T. K. Chan, and S. V. Nghiem, "Soil moisture retrieval from AMSR-E," *IEEE Trans. Geosci. Remote Sens.*, vol. 41, no. 2, pp. 215–229, Feb. 2003.
- [8] C. S. Draper, J. P. Walker, P. J. Steinle, R. A. De Jeu, and T. R. Holmes, "An evaluation of AMSR-E derived soil moisture over Australia," *Remote Sens. Environ.*, vol. 113, no. 4, pp. 703–710, Apr. 2009.
- [9] T. J. Jackson *et al.*, "Validation of advanced microwave scanning radiometer soil moisture products," *IEEE Trans. Geosci. Remote Sens.*, vol. 48, no. 12, pp. 4256–4272, Dec. 2010.
- [10] K. Imaoka *et al.*, "Global change observation mission (GCOM) for monitoring carbon, water cycles, and climate change," *Proc. IEEE*, vol. 98, no. 5, pp. 717–734, May 2010.
- [11] T. Oki, K. Imaoka, and M. Kachi, "AMSR instruments on GCOM-W1/2: Concepts and applications," in *Proc. Geosci. Remote Sens. Symp.*, 2010, pp. 1363–1366.
- [12] R. Bindlish *et al.*, "GCOM-W AMSR2 soil moisture product validation using core validation sites," *IEEE J. Sel. Topics Appl. Earth Observ. Remote Sens.*, vol. 11, no. 1, pp. 209–219, Jan. 2018.
- [13] H. Kim *et al.*, "Global-scale assessment and combination of SMAP with ASCAT (active) and AMSR2 (passive) soil moisture products," *Remote Sens. Environ.*, vol. 204, pp. 260–275, Jan. 2018.
- [14] Y. H. Kerr, P. Waldteufel, J. P. Wigneron, J. A. M. J. Martinuzzi, J. Font, and M. Berger, "Soil moisture retrieval from space: The soil moisture and ocean salinity (SMOS) mission," *IEEE Trans. Geosci. Remote Sens.*, vol. 39, no. 8, pp. 1729–1735, Aug. 2001.
- [15] Y. H. Kerr *et al.*, "The SMOS soil moisture retrieval algorithm," *IEEE Trans. Geosci. Remote Sens.*, vol. 50, no. 5, pp. 1384–1403, May 2012.
- [16] T. J. Jackson *et al.*, "Validation of soil moisture and ocean salinity (SMOS) soil moisture over watershed networks in the US," *IEEE Trans. Geosci. Remote Sens.*, vol. 50, no. 5, pp. 1530–1543, May 2012.
- [17] S. K. Chan *et al.*, "Assessment of the SMAP passive soil moisture product," *IEEE Trans. Geosci. Remote Sens.*, vol. 54, no. 8, pp. 4994–5007, Aug. 2016.
- [18] A. Colliander *et al.*, "Validation of SMAP surface soil moisture products with core validation sites," *Remote Sens. Environ.*, vol. 191, pp. 215–231, Mar. 2017.
- [19] S. K. Chan *et al.*, "Development and assessment of the SMAP enhanced passive soil moisture product," *Remote Sens. Environ.*, vol. 204, pp. 931–941, Jan. 2018.
- [20] H. Kim, and V. Lakshmi, "Use of cyclone global navigation satellite system (CYGNSS) observations for estimation of soil moisture," *Geophys. Res. Lett.*, vol. 45, no. 16, pp. 8272–8282, Aug. 2018.
- [21] R. Bindlish, T. Jackson, M. Cosh, T. Zhao, and P. O'Neill, "Global soil moisture from the Aquarius/SAC-D satellite: Description and initial assessment," *IEEE Geosci. Remote Sens. Lett.*, vol. 12, no. 5, pp. 923–927, May 2015.
- [22] D. Li, *et al.*, "First evaluation of aquarius soil moisture products using in situ observations and GLDAS model simulations," *IEEE J. Sel. Topics Appl. Earth Observ. Remote Sens.*, vol. 8, no. 12, pp. 5511–5525, Dec. 2015.
- [23] T. Schmugge, P. E. O'Neill, and J. R. Wang, "Passive microwave soil moisture research," *IEEE Trans. Geosci. Remote Sens.*, vol. GE-24, no. 1, pp. 12–22, Jan. 1986.
- [24] T. Schmugge and T. J. Jackson, "Mapping surface soil moisture with microwave radiometers," *Meteorol. Atmospheric Phys.*, vol. 54, no. 1–4, pp. 213–223, 1994.
- [25] V. Lakshmi, "Remote sensing of soil moisture," *ISRN Soil Sci.*, vol. 2013, 2013, Art. no. 424178.
- [26] V. Lakshmi, *Remote Sensing of the Terrestrial Water Cycle*. vol. 206. New York, NY, USA: Wiley, 2014.
- [27] D. Bradley *et al.*, "Radio-frequency interference (RFI) mitigation for the soil moisture active/passive (SMAP) radiometer," in *Proc. IEEE Int. Geosci. Remote Sens. Symp.*, 2010, pp. 2015–2018.
- [28] M. W. Spencer, C. W. Chen, H. Ghaemi, S. F. Chan, and J. E. Belz, "RFI characterization and mitigation for the SMAP radar," *IEEE Trans. Geosci. Remote Sens.*, vol. 51, no. 10, pp. 4973–4982, Oct. 2013.
- [29] J. R. Piepmeier *et al.*, "Radio-frequency interference mitigation for the soil moisture active passive microwave radiometer," *IEEE Trans. Geosci. Remote Sens.*, vol. 52, no. 1, pp. 761–775, Oct. 2013.
- [30] D. M. Le Vine, A. J. Griffis, C. T. Swift, and T. J. Jackson, "ESTAR: A synthetic aperture microwave radiometer for remote sensing applications," *Proc. IEEE*, vol. 82, no. 12, pp. 1787–1801, Dec. 1994.
- [31] J. Peng, A. Loew, O. Merlin, and N. E. Verhoest, "A review of spatial downscaling of satellite remotely sensed soil moisture," *Rev. Geophys.*, vol. 55, no. 2, pp. 341–366, Mar. 2017.
- [32] S. Sabaghy, J. P. Walker, L. J. Renzullo, and T. J. Jackson, "Spatially enhanced passive microwave derived soil moisture: Capabilities and opportunities," *Remote Sens. Environ.*, vol. 209, pp. 551–580, May 2018.
- [33] M. Piles *et al.*, "Downscaling SMOS-derived soil moisture using MODIS visible/infrared data," *IEEE Trans. Geosci. Remote Sens.*, vol. 49, no. 9, pp. 3156–3166, Sep. 2011.
- [34] M. Piles *et al.*, "A downscaling approach for SMOS land observations: Evaluation of high-resolution soil moisture maps over the Iberian Peninsula," *IEEE J. Sel. Topics Appl. Earth Observ. Remote Sens.*, vol. 7, no. 9, pp. 3845–3857, Sep. 2014.
- [35] B. Fang, V. Lakshmi, R. Bindlish, T. J. Jackson, M. Cosh, and J. Basara, "Passive microwave soil moisture downscaling using vegetation index and skin surface temperature," *Vadose Zone J.*, vol. 12, no. 3, pp. 1–19, Nov. 2013.
- [36] A. Colliander *et al.*, "Spatial downscaling of SMAP soil moisture using MODIS land surface temperature and NDVI during SMAPVEX15," *IEEE Geosci. Remote Sens. Lett.*, vol. 14, no. 11, pp. 2107–2111, Nov. 2017.
- [37] B. Fang, V. Lakshmi, R. Bindlish, T. J. Jackson, and P. W. Liu, "Evaluation and validation of a high spatial resolution satellite soil moisture product over the continental United States," *J. Hydrol.*, vol. 588, Sep. 2020, Art. no. 125043.
- [38] W. Zhao and A. Li, "A downscaling method for improving the spatial resolution of AMSR-E derived soil moisture product based on MSG-SEVIRI data," *Remote Sens.*, vol. 5, no. 12, pp. 6790–6811, 2013.
- [39] J. D. Bolten, V. Lakshmi, and E. G. Njoku, "Soil moisture retrieval using the passive/active L- and S-band radar/radiometer," *IEEE Trans. Geosci. Remote Sens.*, vol. 41, no. 12, pp. 2792–2801, Dec. 2003.
- [40] U. Narayan, V. Lakshmi, and E. G. Njoku, "Retrieval of soil moisture from passive and active L/S band sensor (PALS) observations during the soil moisture experiment in 2002 (SMEX02)," *Remote Sens. Environ.*, vol. 92, no. 4, pp. 483–496, Sep. 2004.
- [41] U. Narayan, V. Lakshmi, and T. J. Jackson, "High-resolution change estimation of soil moisture using L-band radiometer and radar observations made during the SMEX02 experiments," *IEEE Trans. Geosci. Remote Sens.*, vol. 44, no. 6, pp. 1545–1554, Jun. 2006.
- [42] U. Narayan and V. Lakshmi, "Characterizing subpixel variability of low resolution radiometer derived soil moisture using high resolution radar data," *Water Resour. Res.*, vol. 44, no. 6, Jun. 2008, Art. no. W06425.
- [43] X. Zhan *et al.*, "Fusing microwave and optical satellite observations for high resolution soil moisture data products," in *Proc. IEEE Int. Geosci. Remote Sens. Symp.*, 2017, pp. 2519–2522.
- [44] B. Fang, V. Lakshmi, T. Jackson, R. Bindlish, and A. Colliander, "Passive/active microwave soil moisture change disaggregation using SMAPVEX12 data," *J. Hydrol.*, vol. 574, pp. 1085–1098, Jul. 2019.
- [45] B. Fang and V. Lakshmi, "AMSR-E soil moisture disaggregation using MODIS and NLDAS data," *Remote Sens. Terr. Water Cycle*, vol. 206, pp. 277–304, Oct. 2014.
- [46] S. Kim, K. Balakrishnan, Y. Liu, F. Johnson, and A. Sharma, "Spatial disaggregation of coarse soil moisture data by using high-resolution remotely sensed vegetation products," *IEEE Geosci. Remote Sens. Lett.*, vol. 14, no. 9, pp. 1604–1608, Sep. 2017.
- [47] O. Merlin, A. Bitar, J. P. Walker, and Y. Kerr, "An improved algorithm for disaggregating microwave-derived soil moisture based on red, near-infrared and thermal-infrared data," *Remote Sens. Environ.*, vol. 114, no. 10, pp. 2305–2316, Oct. 2010.
- [48] O. Merlin, M. J. Escorihuela, M. A. Mayoral, O. Hagolle, A. A. Bitar, and Y. Kerr, "Self-calibrated evaporation-based disaggregation of SMOS soil moisture: An evaluation study at 3 km and 100 m resolution in Catalunya, Spain," *Remote Sens. Environ.*, vol. 130, pp. 25–38, Mar. 2013.
- [49] V. Mishra *et al.*, "An initial assessment of a SMAP soil moisture disaggregation scheme using TIR surface evaporation data over the continental United States," *Int. J. Appl. Earth Observ. Geoinf.*, vol. 68, pp. 92–104, Jun. 2018.
- [50] J. Peng, J. Niessel, and A. Loew, "Evaluation of soil moisture downscaling using a simple thermal-based proxy—the REMEDHUS network (Spain) example," *Hydrol. Earth Syst. Sci.*, vol. 19, no. 12, pp. 4765–4782, 2015.

- [51] J. Peng, A. Loew, S. Zhang, J. Wang, and J. Niesel, "Spatial downscaling of satellite soil moisture data using a vegetation temperature condition index," *IEEE Trans. Geosci. Remote Sens.*, vol. 54, no. 1, pp. 558–566, Jan. 2016.
- [52] T. Tagesson *et al.*, "Disaggregation of SMOS soil moisture over west Africa using the temperature and vegetation dryness index based on SEVIRI land surface parameters," *Remote Sens. Environ.*, vol. 206, pp. 424–441, Mar. 2018.
- [53] G. Kim, and A. P. Barros, "Downscaling of remotely sensed soil moisture with a modified fractal interpolation method using contraction mapping and ancillary data," *Remote Sens. Environ.*, vol. 83, no. 3, pp. 400–413, Dec. 2002.
- [54] O. Merlin, A. Chehbouni, G. Boulet, and Y. Kerr, "Assimilation of disaggregated microwave soil moisture into a hydrologic model using coarse-scale meteorological data," *J. Hydrometeorol.*, vol. 7, no. 6, pp. 1308–1322, Dec. 2006.
- [55] R. H. Reichle, R. D. Koster, P. Liu, S. P. Mahanama, E. G. Njoku, and M. Owe, "Comparison and assimilation of global soil moisture retrievals from the advanced microwave scanning radiometer for the earth observing system (AMSR-E) and the scanning multichannel microwave radiometer (SMMR)," *J. Geophys. Res., Atmos.*, vol. 112, May 2007, Art. no. D09108.
- [56] S. Sánchez-Ruiz, M. Piles, N. Sánchez, and J. Martínez-Fernández, "Mercè Vall-llossera, and adriano camps combining SMOS with visible and near/shortwave/thermal infrared satellite data for high resolution soil moisture estimates," *J. Hydrol.*, vol. 516, pp. 273–283, Aug. 2014.
- [57] W. Zhao, N. Sánchez, H. Lu, and A. Li, "A spatial downscaling approach for the SMAP passive surface soil moisture product using random forest regression," *J. Hydrol.*, vol. 563, pp. 1009–1024, Aug. 2018.
- [58] R. R. Gillies, W. P. Kustas, and K. S. Humes, "A verification of the 'triangle' method for obtaining surface soil water content and energy fluxes from remote measurements of the normalized difference vegetation index (NDVI) and surface e," *Int. J. Remote Sens.*, vol. 18, no. 15, pp. 3145–3166, 1997.
- [59] T. Carlson, "An overview of the 'triangle method' for estimating surface evapotranspiration and soil moisture from satellite imagery," *Sensors*, vol. 7, no. 8, pp. 1612–1629, 2007.
- [60] K. Mallick, B. K. Bhattacharya, and N. K. Patel, "Estimating volumetric surface moisture content for cropped soils using a soil wetness index based on surface temperature and NDVI," *Agricultural Forest Meteorol.*, vol. 149, no. 8, pp. 1327–1342, Aug. 2009.
- [61] M. Minacapilli, M. Iovino, and F. Blanda, "High resolution remote estimation of soil surface water content by a thermal inertia approach," *J. Hydrol.*, vol. 379, no. 3–4, pp. 229–238, Dec. 2009.
- [62] V. Lakshmi, K. Czajkowski, R. Dubayah, and J. Susskind, "Land surface air temperature mapping using TOVS and AVHRR," *Int. J. Remote Sens.*, vol. 22, no. 4, pp. 643–662, 2001.
- [63] V. Lakshmi, S. Hong, E. E. Small, and F. Chen, "The influence of the land surface on hydrometeorology and ecology: New advances from modeling and satellite remote sensing," *Hydrol. Res.*, vol. 42, no. 2/3, pp. 95–112, 2011.
- [64] C. R. Hain, W. T. Crow, J. R. Mecikalski, M. C. Anderson, and T. Holmes, "An intercomparison of available soil moisture estimates from thermal infrared and passive microwave remote sensing and land surface modeling," *J. Geophys. Res., Atmos.*, vol. 116, no. D15, Aug. 2011, Art. no. D15107.
- [65] B. Fang and V. Lakshmi, "Soil moisture at watershed scale: Remote sensing techniques," *J. Hydrol.*, vol. 516, pp. 258–272, Aug. 2014.
- [66] B. Fang, V. Lakshmi, R. Bindlish, and T. Jackson, "Downscaling of SMAP soil moisture using land surface temperature and vegetation data," *Vadose Zone J.*, vol. 17, no. 1, pp. 1–15, Aug. 2018.
- [67] B. Fang, V. Lakshmi, R. Bindlish, and T. Jackson, "AMSR2 soil moisture downscaling using temperature and vegetation data," *Remote Sens.*, vol. 10, no. 10, pp. 1575, Oct. 2018.
- [68] I. P. Senanayake *et al.*, "An in-situ data based model to down-scale radiometric satellite soil moisture products in the upper hunter region of NSW, Australia," *J. Hydrol.*, vol. 572, pp. 820–838, May 2019.
- [69] C. Dandridge, B. Fang, and V. Lakshmi, "Downscaling of SMAP soil moisture in the lower mekong river basin," *Water*, vol. 12, no. 1, p. 56, 2020.
- [70] D. Matsushima, R. Kimura, and M. Shinoda, "Soil moisture estimation using thermal inertia: Potential and sensitivity to data conditions," *J. Hydrometeorol.*, vol. 13, no. 2, pp. 638–648, Apr. 2012.
- [71] V. Tramutoli, P. Claps, M. Marella, N. Pergola, C. Pietrapertosa, and C. Sileo, *Hydrological Implications of Remotely Sensed Thermal Inertia*, Santa Fe, NM, USA: Iahs Publ., 2001, pp. 207–211.
- [72] M. B. Ek *et al.*, "Implementation of noah land surface model advances in the national centers for environmental prediction operational mesoscale eta model," *J. Geophys. Res., Atmos.*, vol. 108, D22, Nov. 2003, Art. no. 8851.
- [73] J. C. Schaake *et al.*, "An intercomparison of soil moisture fields in the North American land data assimilation system (NLDAS)," *J. Geophys. Res., Atmos.*, vol. 109, no. D1, Jan. 2004, Art. no. D01S90.
- [74] K. E. Mitchell *et al.*, "The multi-institution north american land data assimilation system (NLDAS): Utilizing multiple GCIP products and partners in a continental distributed hydrological modeling system," *J. Geophys. Res., Atmos.*, vol. 109, no. D7, Apr. 2004, Art. no. D07S90.
- [75] C. R. Hain, W. T. Crow, M. C. Anderson, and J. R. Mecikalski, "An ensemble kalman filter dual assimilation of thermal infrared and microwave satellite observations of soil moisture into the Noah land surface model," *Water Resour. Res.*, vol. 48, no. 11, Nov. 2012, Art. no. W11517.
- [76] Y. Xia *et al.*, "Validation of Noah-simulated soil temperature in the North American land data assimilation system phase 2," *J. Appl. Meteorol. Climatol.*, vol. 52, no. 2, pp. 455–471, Feb. 2013.
- [77] C. J. Tucker, "Red and photographic infrared linear combinations for monitoring vegetation," *Remote Sens. Environ.*, vol. 8, no. 2, pp. 127–150, 1979.
- [78] Z. Wan, and Z. L. Li, "A physics-based algorithm for retrieving land-surface emissivity and temperature from EOS/MODIS data," *IEEE Trans. Geosci. Remote Sens.*, vol. 35, no. 4, pp. 980–996, Jul. 1997.
- [79] Z. Wan, Y. Zhang, Q. Zhang, and Z. L. Li, "Validation of the land-surface temperature products retrieved from terra moderate resolution imaging spectroradiometer data," *Remote Sens. Environ.*, vol. 83, no. 1–2, pp. 163–180, Nov. 2002.
- [80] J. Pedelty *et al.*, "Generating a long-term land data record from the AVHRR and MODIS instruments," in *Proc. Geosci. Remote Sens. Symp.*, 2007, pp. 1021–1025.
- [81] F. Bédard, S. Crump, and J. Gaudreau, "A comparison between terra MODIS and NOAA AVHRR NDVI satellite image composites for the monitoring of natural grassland conditions in Alberta, Canada," *Can. J. Remote Sens.*, vol. 32, no. 1, pp. 44–50, Jun. 2006.
- [82] C. Cao, F. J. De Luccia, X. Xiong, R. Wolfe, and F. Weng, "Early on-orbit performance of the visible infrared imaging radiometer suite onboard the Suomi national polar-orbiting partnership (S-NPP) satellite," *IEEE Trans. Geosci. Remote Sens.*, vol. 52, no. 2, pp. 1142–1156, May 2013.
- [83] J. C. Price, "Estimating surface temperatures from satellite thermal infrared data—A simple formulation for the atmospheric effect," *Remote Sens. Environ.*, vol. 13, no. 4, pp. 353–361, Sep. 1983.
- [84] T. Islam, G. C. Hulley, N. K. Malakar, R. G. Radocinski, P. C. Guillevic, and S. J. Hook, "A physics-based algorithm for the simultaneous retrieval of land surface temperature and emissivity from VIIRS thermal infrared data," *IEEE Trans. Geosci. Remote Sens.*, vol. 55, no. 1, pp. 563–576, Oct. 2016.
- [85] N. K. Malakar and G. C. Hulley, "A water vapor scaling model for improved land surface temperature and emissivity separation of MODIS thermal infrared data," *Remote Sens. Environ.*, vol. 182, pp. 252–264, Sep. 2016.
- [86] S. Saha *et al.*, "The NCEP climate forecast system version 2," *J. Climate*, vol. 27, no. 6, pp. 2185–2208, 2014.
- [87] A. Y. Hou *et al.*, "The global precipitation measurement mission," *Bull. Amer. Meteorol. Soc.*, vol. 95, no. 5, pp. 701–722, May 2014.
- [88] G. J. Huffman *et al.*, "NASA global precipitation measurement (GPM) integrated multi-satellite retrievals for GPM (IMERG)," *Algorithm Theor. Basis Document, Version*, vol. 4, p. 26, 2015.
- [89] W. A. Dorigo *et al.*, "The international soil moisture network: A data hosting facility for global in situ soil moisture measurements," *Hydrol. Earth System Sci.*, vol. 15, no. 5, pp. 1675–1698, May 2011.
- [90] W. A. Dorigo *et al.*, "Global automated quality control of in situ soil moisture data from the international soil moisture network," *Vadose Zone J.*, vol. 12, no. 3, p. 0097, Aug. 2013.
- [91] A. Gruber, W. A. Dorigo, S. Zwieback, A. Xaver, and W. Wagner, "Characterizing coarse-scale representativeness of in situ soil moisture measurements from the international soil moisture network," *Vadose Zone J.*, vol. 12, no. 2, pp. 1–16, May 2013.
- [92] G. L. Schaefer, M. H. Cosh, and T. J. Jackson, "The USDA natural resources conservation service soil climate analysis network (SCAN)," *J. Atmos. Ocean. Technol.*, vol. 24, no. 12, pp. 2073–2077, 2007.

- [93] M. Zreda *et al.*, "COSMOS: The cosmic-ray soil moisture observing system," *Hydrol. Earth System Sci.*, vol. 16, no. 11, pp. 4079–4099, Nov. 2012.
- [94] J. E. Bell *et al.*, "US climate reference network soil moisture and temperature observations," *J. Hydrometeorol.*, vol. 14, no. 3, pp. 977–988, Jun. 2013.
- [95] X. Han, R. Jin, X. Li, and S. Wang, "Soil moisture estimation using cosmic-ray soil moisture sensing at heterogeneous farmland," *IEEE Geosci. Remote Sens. Lett.*, vol. 11, no. 9, pp. 1659–1663, Apr. 2014.
- [96] E. J. Coopersmith, M. H. Cosh, J. E. Bell, and W. T. Crow, "Multi-profile analysis of soil moisture within the US climate reference network," *Vadose Zone J.*, vol. 15, no. 1, pp. 1–8, 2016.
- [97] T. R. Karl and W. J. Koss, "Regional and national monthly, seasonal, and annual temperature weighted by area, 1895–1983," *Nat. Ocean. Atmospheric Admin.*, Washington, DC, USA, 1984.
- [98] B. Fang, P. Kansara, C. Dandridge, and V. Lakshmi, "Drought monitoring using high spatial resolution soil moisture data over Australia in 2015–2019," *J. Hydrol.*, vol. 594, Mar. 2021, Art. no. 125960.
- [99] S. Hong, V. Lakshmi, E. E. Small, F. Chen, M. Tewari, and K. W. Manning, "Effects of vegetation and soil moisture on the simulated land surface processes from the coupled WRF/Noah model," *J. Geophys. Res., Atmos.*, vol. 114, no. D18, Sep. 2009, Art. no. D18118.
- [100] R. H. Reichle *et al.*, "Assessment of the SMAP level-4 surface and root-zone soil moisture product using in situ measurements," *J. Hydrometeorol.*, vol. 18, no. 10, pp. 2621–2645, 2017.
- [101] Z. Wan, "New refinements and validation of the MODIS land-surface temperature/emissivity products," *Remote Sens. Environ.*, vol. 112, no. 1, pp. 59–74, Jan. 2008.
- [102] M. H. Cosh, T. J. Jackson, R. Bindlish, and J. H. Prueger, "Watershed scale temporal and spatial stability of soil moisture and its role in validating satellite estimates," *Remote Sens. Environ.*, vol. 92, no. 4, pp. 427–435, Sep. 2004.
- [103] J. S. Famiglietti, D. Ryu, A. A. Berg, M. Rodell, and T. J. Jackson, "Field observations of soil moisture variability across scales," *Water Resour. Res.*, vol. 44, no. 1, Jan. 2008, Art. no. W01423.
- [104] L. Fang, C. R. Hain, X. Zhan, and M. C. Anderson, "An inter-comparison of soil moisture data products from satellite remote sensing and a land surface model," *Int. J. Appl. Earth Observ. Geoinf.*, vol. 48, pp. 37–50, Jun. 2016.



Bin Fang received the Ph.D. degree in geological sciences from the University of South Carolina, Columbia, SC, USA, in 2015.

He is currently a Postdoctoral Researcher with the Department of Engineering Systems and Environment, University of Virginia, Charlottesville, VA, USA. His research interests include the remote sensing applications in hydrology, agriculture and ecology, as well as soil moisture data assimilation into hydrological models. His current research focuses on using passive microwave and visible/near-infrared

satellite data for soil moisture measuring and hydrologic extremes monitoring. These studies range from watershed scale to continental scale using the data from airborne sensors as well as satellites.



Venkat Lakshmi (Senior Member, IEEE) the bachelor's degree in civil engineering from the University of Roorkee, Roorkee, India, in 1987 and the Doctorate degree in civil and environmental engineering from Princeton University, Princeton, NJ, USA, in 1996.

From 1996 to 1999, he was a Research Scientist with the Laboratory for the Atmospheres, NASA Goddard Space Flight Center. He is currently a Professor with the Department of Engineering Systems and the Environment, University of Virginia, Charlottesville, VA, USA. He was a Cox Visiting Professor with Stanford University, during 2006–2007 and 2015–2016; and the Program Director for hydrologic sciences with the National Science Foundation, during 2017–2018. He has more than 120 peer-reviewed articles and 400 presentations and thesis supervisor for 25 graduate students. His research interest include catchment hydrology, satellite data validation and assimilation, field experiments, land-atmosphere interactions, satellite data downscaling, vadose zone, and water resources.

Dr. Lakshmi is a Fellow of the American Society of Civil Engineers and Geological Society of America. He is currently an Editor for *Vadose Zone Journal* and the Founding Editor-In-Chief of *Remote Sensing in Earth System Science* (Springer Journals). He has served on the National Academies Panel for the Decadal Survey of Earth Observations from Space (NASA) and the Chair of the planning committee for Groundwater Recharge and Flow: Approaches and Challenges for Monitoring and Modeling Using Remotely Sensed Data (NGA). He is currently a member of the Water Science and Technology Board, National Academy of Sciences.



Michael H. Cosh (Senior Member, IEEE) received the Ph.D. degree in civil and environmental engineering from Cornell University, Ithaca, NY, USA, in 2002.

He is a Research Hydrologist with the U.S. Department of Agriculture, Agricultural Research Service, Hydrology and Remote Sensing Laboratory, Beltsville, MD, USA. His current research interests include the monitoring of soil moisture from both in situ resources and satellite products. He conducts research on satellite calibration and validation for

such missions as the soil moisture active passive and soil moisture ocean salinity missions. His current research interests include the monitoring of soil moisture from both in situ resources and satellite products

Dr. Cosh is a Fellow of the American Society of Agronomy.



Christopher Hain received the bachelor's degree in meteorology from Millersville University, Millersville, PA, USA, in 2004, and the master's degree in atmospheric science and the Doctorate degree in atmospheric science from the University of Alabama in Huntsville, Huntsville, AL, USA, in 2007 and 2010, respectively.

From 2010 to 2016, he was with the Earth System Science Interdisciplinary Center, University of Maryland. He currently a Research Scientist at NASA's Marshall Space Flight Center and is the Project Scientist for the Short-Term Prediction Research and Transition Center. He has played a significant role in the development of the Atmosphere Land Exchange Inverse (ALEXI) model in ongoing collaboration with scientists at the USDA-ARS Hydrology and Remote Sensing Lab; ALEXI is currently used to monitor continental evapotranspiration, soil moisture, and drought. He has authored or co-authored more than 100 peer-reviewed articles and more than 75 presentations within the scientific community. His research interests include interested in thermal infrared remote sensing with applications in surface energy balance modeling, soil moisture retrieval, hydrologic data assimilation and drought monitoring.